Induced Polarization of Carbonates

Neha Panwar, André Revil, Ravi Sharma, Myriam Schmutz, Pierre-Allain Duvillard, Bruno Garcia, Adrian Cerepi, Ruben Garcia-Artigas, Pierre Vaudelet, Emmanuel Malet, et al.

JGR Solid Earth

RESEARCH ARTICLE
10.1029/2021JB022029

Induced Polarization of Carbonates

N. Panwar[1,2], A. Revil[2], R. Sharma[1], M. Schmutz[3], P.A. Duvillard[2,4], B. Garcia[5], A. Cerepi[3], R. Garcia-Artigas[6,7], P. Vaudelet[8], E. Malet[2], and S. Jaillet[2]

[1]Indian Institute of Technology, Roorkee, Uttarakhand, India, [2]Université Grenoble Alpes, Université Savoie Mont-Blanc, CNRS, UMR 5204, EDYTEM, Le Bourget-du-Lac, France, [3]Bordeaux INP—Université Bordeaux Montaigne, Talence, France, [4]Now at STYX4D, Le Bourget-du-Lac, France, [5]IFP Energies Nouvelles, Rueil-Malmaison, France, [6]Water Research Institute (IdRA), University of Barcelona, Barcelona, Spain, [7]Faculty of Earth Sciences, University of Barcelona, Barcelona, Spain, [8]Naga Geophysics, Le Bourget-du-Lac, France

Key Points:

- The surface of carbonate grains is charged and therefore susceptible to get polarized in an electrical field
- Carbonate rocks display induced polarization in the laboratory and in the field
- The polarization of carbonates is explained by the dynamic Stern layer concept

Correspondence to:
A. Revil,
andre.revil@univ-smb.fr

Citation:
Panwar, N., Revil, A., Sharma, R., Schmutz, M., Duvillard, P. A., Garcia, B., et al. (2021). Induced polarization of carbonates. *Journal of Geophysical Research: Solid Earth*, *126*, e2021JB022029. https://doi.org/10.1029/2021JB022029

Received 8 MAR 2021
Accepted 20 APR 2021

Abstract Complex conductivity measurements of carbonate rocks are scarce despite the occurrence of these rocks at the surface of the Earth. The complex conductivity spectra of 57 carbonate samples were measured in a broad frequency range and at four salinities (NaCl). A simple model of induced polarization is developed to be applied to induced polarization measurements in the field. The in-phase conductivity (related to conduction) is reported as a function of the pore water conductivity to determine the (intrinsic) formation factor and the surface conductivity. The surface conductivity and the normalized chargeability are linearly correlated to the specific surface area divided by the tortuosity of the pore space. This observation is consistent with a dynamic Stern layer polarization model, the Stern layer being the inner layer of the electrical double layer coating the grains. The quadrature conductivity is observed to be proportional to the measured normalized chargeability in agreement with the prediction of the constant phase model. The effect of the texture is discussed and we observe a power-law relationship between the permeability and the formation factor. Then, we illustrate how this model can be applied to field data performed over a carbonate syncline in the French Alps. A 1.9 km long profile is used to separate the glacial till infilling the depression from the underlying limestones in terms of induced polarization properties. The induced polarization survey allows imaging the water content and the specific surface area of the formations down to a depth of 220 m.

1. Introduction

Carbonate rocks (i.e., rocks containing at least 50% of calcite or dolomite) are among the most common rocks at the surface of the Earth (~20% of sedimentary rocks) and form an important source of drinkable water aquifers (e.g., Ford & Williams, 2007) and 40% of the oil and gas reservoirs (e.g., Brigaud et al., 2014). The electrical conductivity of carbonate rocks has been broadly investigated in the literature (e.g., Cerepi, 2004; Focke & Munn, 1987; Regnet et al., 2019; Winn, 1957). It is generally assumed that conductivity of these rocks is dominated by the bulk conductivity associated with conduction in the pore water located in the connected pore network. Similarly, the Maxwell-Wagner polarization of carbonate rocks (occurring at intermediate frequency range ~100 Hz-10 MHz) has also been broadly described (e.g., Hizem et al., 2008). The Maxwell-Wagner or interfacial polarization is related to the discontinuity of the displacement current density at the interface between the different phases of a porous composite. That said, little quantitative investigations have been performed regarding their induced (low-frequency, <~10 kHz) polarization properties despite the need for a simple physics-based model of induced polarization in carbonate rocks that can be applied to field data.

Induced polarization refers to the reversible charge accumulation in charged porous media under the influence of a primary electrical field and at low frequencies (i.e., typically <10 kHz, e.g., Abdulsamad et al., 2019; Börner, 1992). These charge accumulations occur mostly at grain or pore scales (e.g., Weller et al., 2015), which correspond to polarization length scales controlling a distribution of relaxation times. In the field, induced polarization imaging is nowadays broadly used in the realm of hydrogeophysics (Binley & Kemna, 2005; Binley et al., 2015; Kemna et al., 2012) including for landfill characterization (Flores Orozco et al., 2011, 2020), water-filtration system characterization in terms of bio-clogging (Garcia-Artigas et al., 2020), and the characterization of areas prone to landslides (Flores Orozco et al., 2018; Revil et al., 2020) and volcanoes (Revil et al., 2017b). For soils (Revil et al., 2017a), siliciclastic rocks (Revil

et al., 2018), and volcanic rocks (Ghorbani et al., 2018; Revil et al., 2017b, 2017c), the dynamic Stern layer polarization model has proved to be very effective in describing their complex conductivity spectra. The Stern layer has also been observed for calcite and the mobility of the counterions in the Stern layer independently assessed (Ricci et al., 2013).

Leroy et al. (2017) developed the first quantitative model based on an electrical double layer approach to explain the spectral induced polarization associated with the precipitation of calcite in porous media. However this model was not tested on a broad range of carbonate core samples and does not provide a simple, yet efficient, model to quantity the induced polarization properties of carbonate rocks. With the exception of the work by Leroy et al. (2017), other works related to the complex conductivity of carbonate rocks have been performed but remain qualitative (see for instance Halisch et al., 2018; Hupfer et al., 2017; Li et al., 2016; Norbisrath et al., 2018; Saneiyan et al., 2021, and Wu et al., 2010, for the induced polarization associated with bio-controlled calcite precipitation). A quantitative and yet simple model describing the complex conductivity of carbonates has been therefore missing. Such model is however required to interpret galvanometric field-based induced polarization data below 100 Hz (above this critical frequency, electromagnetic coupling effects complicate the observed signals).

The key scientific questions we want to answer in this work are the following (a) is surface conductivity really negligible in natural carbonate rocks, which can include clay minerals in their composition? (b) Can the dynamic Stern layer model of grain polarization of siliciclastic rocks be applied to carbonate rocks? (c) If yes, what are the values of the two apparent mobilities B and λ entering this model? (d) What is the effect of texture on the electrical properties of interest and can we predict permeability of carbonate rocks using induced polarization? (e) How to use quantitatively induced polarization in the field (below 100 Hz) to characterize carbonate aquifers to estimate their water content? (f) Can we neglect the Maxwell-Wagner polarization of carbonate rocks below 100 Hz?

In order to respond to these questions, we developed a new data set using a representative number of 57 core samples of carbonate rocks. These samples were saturated with brines at three or four distinct salinities (NaCl) depending on the batch. The induced polarization measurements were performed at atmospheric pressure and at 25°C. The petrophysical model is then applied to galvanometric field induced polarization data obtained along a profile in the French Alps.

2. Petrophysics

Induced polarization refers to the reversible storage of electrical charges in porous materials under the influence of an applied electrical field. Carbonate rocks are characterized by a variety of textures (Figures 1 and 2). In the present paper, we are interested especially by porous carbonate rocks, unfractured and with limited vuggy porosity (see Figure 2 for some explanations regarding the occurrence of vuggy porosity associated with the presence of very large pores, >0.5 mm). Low frequency (induced) polarization (typically below 1 kHz) is associated with the existence of an electrical double layer (Gouy, 1910; Stern, 1924) coating the surface of the mineral grains. A sketch of the electrical double layer of calcite is shown in Figure 3. It comprises the charged mineral surafce, the Stern layer of mobile sorbed counterions and coions, and the diffuse layer, Calcite mineral surface is charged because of a large variety of chemical reactions in presence of water. To describe these chemical reactions, a speciation model is required. The surface charge is counterbalanced by charges located in a Stern layer of sorbed counterions plus a diffuse layer in which the co-ions and counterions are tied to the mineral surface only through Coulombic interactions. The modeling of the electrical double layer of calcite is challenging because of the variety of surface sites and potential determining ions forming inner- and outer-sphere complexes with the mineral surface (e.g., Heberling et al., 2011, 2014; Li et al., 2016; Stipp, 1999; van Capellen et al., 1993; Wolthers et al., 2008).

Because of the low-frequency polarization of carbonate rocks, we observe a phase lag between the electrical field and the injected electrical current. Therefore, the low-frequency electrical conductivity spectrum of a charged porous rock is described both by an amplitude $|\sigma|$ (expressed in S m^{-1}) and a phase lag, φ (expressed in rad), which vary with the frequency of the applied electrical field/current (see Maineult et al., 2018). Alternatively, we can write the conductivity as a complex number:

$$\sigma^*(\omega) = |\sigma| e^{i\varphi} = \sigma'(\omega) + i\sigma''(\omega) \quad (1)$$

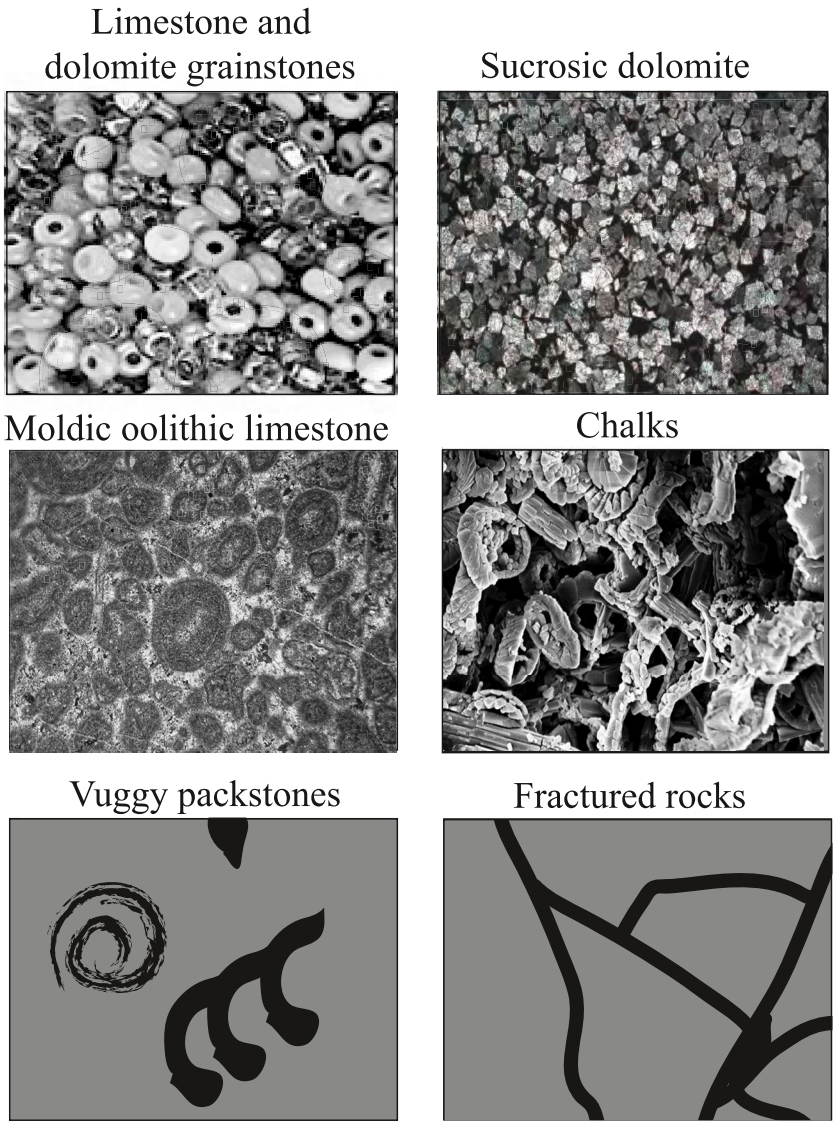

Figure 1. Types of carbonate rocks. The vuggy and fractures limestones are characterized by macroscopic heterogeneities plus a porous matrix. In the present study, we are not interested by vuggy and fractured limestones (modified from Focke & Munn, 1987).

where $i^2 = -1$ and ω denote the angular frequency (rad s^{-1}), σ' and σ'' correspond to the in-phase (real) and quadrature (imaginary) conductivity, respectively. The real part of σ^* denotes the in-phase conductivity, that is, the conductivity for a phase lag equals to zero. The absence of phase lag means ipse facto that there is no polarization and therefore the in-phase conductivity characterizes the conduction process only. By conduction, we mean the drift of the charge carriers (here anion and cations) under the action of an electrical field. The imaginary part of σ^* (out-of-phase component) characterizes the polarization process here associated with the accumulation of charge carriers at the polarization length scales discussed above. Fundamentally, the existence of a phase lag at low frequencies is due to the control exerted by electrochemical potential gradients on the migration of the charge carriers. In other words, charge carriers can accumulate at some polarization length scales in the material and diffuse back in their concentration gradients in addition to move under the influence of the Coulombic field associated with the applied electrical field.

In calcite and clays, a large proportion of the counterions of the electrical double layer is located in the Stern layer (see Figure 3, e.g., Leroy & Revil, 2009; Leroy et al., 2017). The dynamic Stern layer concept provides

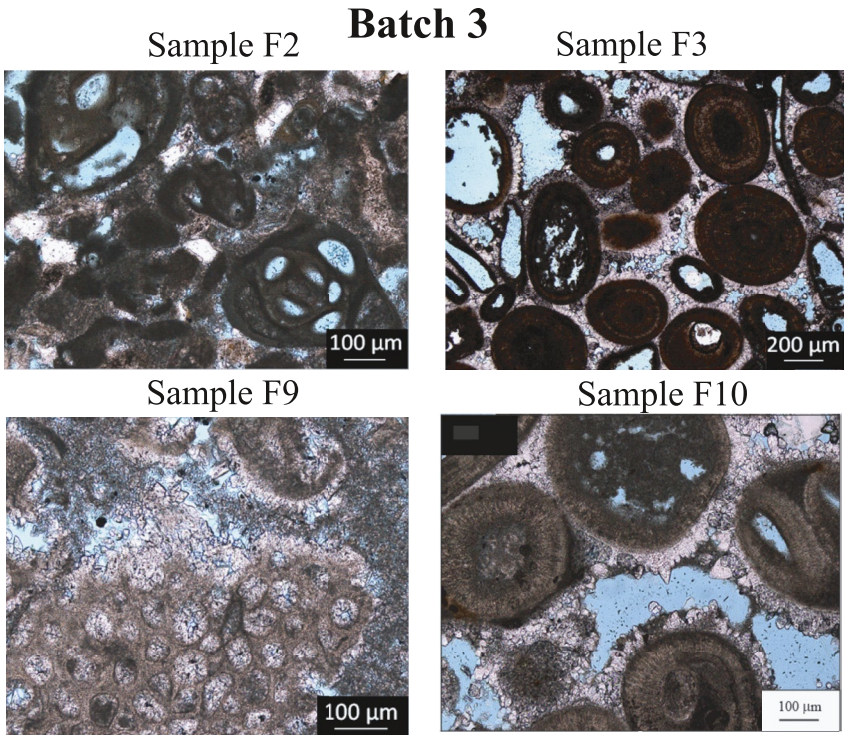

Figure 2. Thin sections revealing the fine porous geometry (in blue) of few selected carbonate core samples from batch 3: Sample F2 is a packstone with primary intraparticular porosity in miliolidae; sample F3 is a grainstone with primary interparticular porosity and secondary vuggy porosity; sample F9 is a packstone with microporosity; sample F10 is a grainstone with both primary interparticular porosity and secondary dissolution porosity.

a mechanistally based and testable model to understand induced polarization (Revil et al., 2017a), which is simple enough to be applicable in field conditions (Revil et al., 2020).

The model used below focus on the induced polarization effect and we do not attempt to model the Maxwell-Wagner polarization effect in this paper. The reason is that we are looking for a simple induced polarization model able to explain field galvanometric induced polarization data that are usually limited at 100 Hz because of spurious electromagnetic coupling effects. We consider ipse facto that below 100 Hz, the induced polarization dominates the Maxwell-Wagner polarization. This point will be discussed further below to the light of the laboratory measurements. Revil et al. (2017a and references therein) developed a comprehensive model able to conceptualize the complex conductivity σ^* of partially water-saturated soils. In this framework, the complex conductivity of a water-saturated carbonate rock could be written as

$$\sigma^*\left(\omega\right) = \sigma_\infty - M_n \int_0^\infty \frac{h\left(\tau\right)}{1+\left(i\omega\tau\right)^{1/2}} d\tau + i\omega\epsilon_\infty \tag{2}$$

$$\sigma_\infty = \phi^m \sigma_w + \phi^{m-1} \rho_g B Q_S \, S_{Sp} \tag{3}$$

$$\sigma_0 = \phi^m \sigma_w + \phi^{m-1} \rho_g \left(B - \lambda\right) Q_S \, S_{Sp} \tag{4}$$

$$M_n = \phi^{m-1} \rho_g \lambda \, Q_S \, S_{Sp} \tag{5}$$

where $h\left(\tau\right)$ corresponds to a kernel and denotes the probability density for the relaxation time τ (in s) in induced polarization, ϵ_∞ (in F m^{-1}) corresponds to the permittivity of the material (in reality the low-frequency bound of the Maxwell-Wagner polarization, see Vinegar & Waxman, 1984 for a detailed discussion),

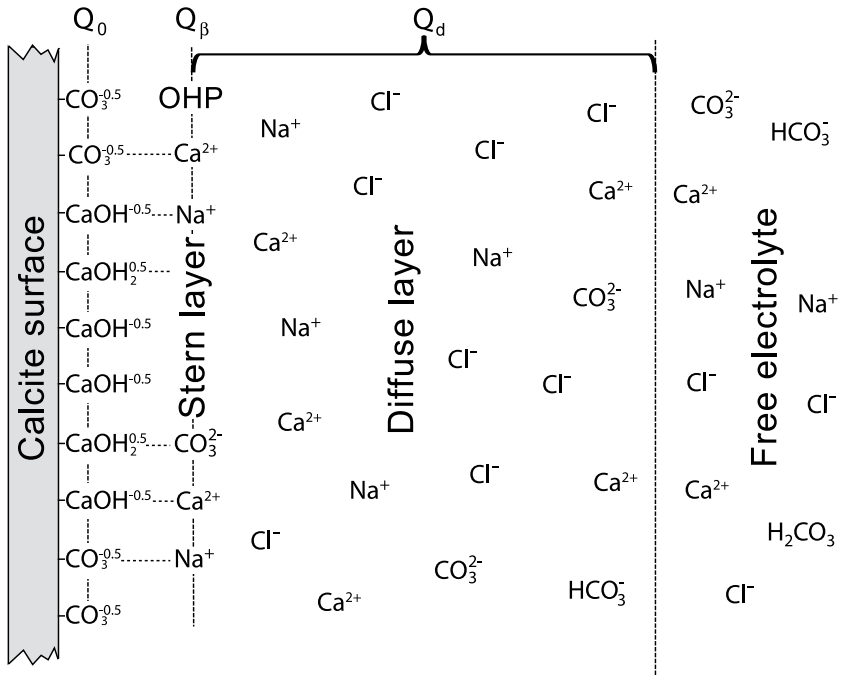

Figure 3. Electrical double layer of the surface of calcite in contact with a sodium chloride (NaCl) solution. OHP stands for the outer Helmholtz plane. The quantities Q_0, Q_β, and Q_d (in C m^{-2}) represent the equivalent surface charge density for the mineral surface, the Stern layer (Stern, 1924), and the Gouy-Chapman diffuse layer (see Gouy, 1910), respectively (adapted from Leroy et al., 2017). Since the surface charge density $Q_S = Q_\beta$, and Q_d and since the sum of the three charge densities are equal to zero (electro-neutrality condition), we have $Q_S = -Q_0$.

σ_∞ (S m^{-1}) defines the instantaneous (high-frequency) conductivity for induced polarization, σ_0 (S m^{-1}) corresponds to the direct current (DC) conductivity, $M_n \equiv \sigma_\infty - \sigma_0$ (S m^{-1}) is the normalized chargeability contribution associated with induced polarization, ϕ (dimensionless) denotes the (connected) porosity, ρ_g the grain density (for calcite 2,710 kg m^{-3}, for aluminosilicates and silicates typically 2,650 kg m^{-3}), Q_S denotes the surface charge density (total charge per unit surface area of the grains, in C m^{-2}), and S_{Sp} denotes the specific surface area of the material (expressed in m^2 kg^{-1}), B and λ (both in m^{2}s^{-1}V^{-1}) denote the apparent mobilities of the counterions for surface conduction (in the electrical double layer) and polarization, respectively. These two mobilities can be related to the intrinsic drift mobilities of the counterions in the Stern and diffuse layers and to the relative fraction of counterions in the Stern layer as discussed in Revil et al. (2017a) and references therein. That said, such description is not required in the present paper. If, however, one needs to connect the present model to a complete speciation model of carbonate rocks, the same approach as developed for silica and aluminosilicates in Leroy et al. (2008) and Leroy and Revil (2009) can easily be implemented.

High and low frequencies are here defined with respect to the distribution of the relaxation times defining $h(\tau)$ and so they refer to the induced polarization only. Since we are interested by the application of our model in field conditions, below 100 Hz, we choose to simplify the treatment of the Maxwell-Wagner polarization but if needed the differential effective medium theory could be used for a more complete treatment (see for instance de Lima & Sharma, 1992). Surface conductivity denotes the surface conduction in the electrical double layer (e.g., Friedman, 2005) and the DC and instantaneous surface conductivities are written from Equations 3 and 4 as $\sigma_S^0 = \phi^{m-1}\rho_g\left(B - \lambda\right)Q_S\, S_{Sp}$ and $\sigma_S^\infty = \phi^{m-1}\rho_g B Q_S\, S_{Sp}$, respectively.

A dimensionless number R was introduced by Revil et al. (2017a, 2017b, 2017c) as $R = \lambda / B$. This dimensionless number represents also the ratio between the the normalized chargeability and the instantaneous surface conductivity. In addition, since $\lambda << B$, the DC surface conductivity is close to the instantaneous surface conductivity. Since R is a universal constant (for a given type of counterions) independent of saturation and temperature, it provides a way to separate the bulk conductivity (associated with conduction in the

Table 1
Petrophysical Properties of the Core Samples From Batch 1 (12 samples)

Sample ID	Description	Porosity ϕ (−)	S_{sp} (BET) (m^2/g)	k (m^2)
I3b	Limestone	0.051	15.45	–
I24	Limestone	0.18	21.29	49E−15
I51	Limestone	0.16	22.48	3.7E−15
I21	Limestone	0.09	–	0.23E−15
I42b	Limestone	0.13	19.85	22E−15
I42a	Limestone	0.10	7.84	1.6E−15
I18	Limestone	0.18	79.43	2.6E−15
I39	Limestone	0.062	36.51	0.026E−15
I23	Limestone	0.061	–	0.049E−15
I15	Wackestone	0.090	27.41	0.039E−15
I19	Limestone	0.096	–	0.257E−15
I48	Micrite	0.22	76.96	34.64E−15

The quantity k denotes the water permeability measured with a permeameter.

bulk pore space) and surface conductivity as suggested by Kulenkampff and Schopper (1988). The quantities ϕ^m and ϕ^{m-1} represent the inverse of the formation factor F of the porous material and the inverse of the bulk tortuosity of the pore space (product of the intrinsic formation factor F by the connected porosity ϕ).

Another relationship can be derived under the assumption of the constant-phase model, which is a good approximation when the probability density for the relaxation times $h(\tau)$ is broad (see Revil et al., 2017a; Vinegar & Waxman, 1984). Under this assumption, the quadrature conductivity and the change of the in-phase conductivity with the frequency can be interrelated by the following expression (Revil et al., 2017a; Van Voorhis et al, 1973)

$$\sigma''\left(\sqrt{f_1 f_2}\right) \approx -\frac{M_n\left(f_1, f_2\right)}{\alpha} \tag{6}$$

where the quadrature conductivity σ'' is determined at the geometric mean frequency of two frequencies f_1 and f_2 and the (partial) normalized chargeability is defined as the difference between the in-phase conductivity at frequency f_2 ($>f_1$) and the in-phase conductivity at the lower frequency f_1. In the constant phase model, the proportionality factor α can be defined as $\alpha \approx \left(2 / \pi\right)\ln A$ where A is the number of decades between f_1 and f_2 (for 3 decades $A = 10^3$ and $\alpha \approx 4.4$, see details in Revil et al., 2017a, see also Börner, 1992). Typically, we consider that the relaxation times associated with the polarization length scales occur over six orders of magnitude (see Vinegar & Waxman, 1984, for a discussion regarding this point) and therefore the partial chargeability taken over the correct six orders of magnitude corresponds to the total normalized chargeability (Revil et al., 2017a). If the partial normalized chargeability is therefore measured over three orders of magnitude (as done below), we need to multiply the number by 2 to get the total normalized chargeability (since $\alpha \approx \left(2 / \pi\right)\ln A$). To avoid any confusion, it is also important to remember that Equation 6 is based on assumptions that are distinct from those associated with the dynamic Stern layer model mentioned above.

3. Material and Methods

3.1. Carbonate Rocks

Our database is formed by five batches. The samples of batch 1 and batch 2 (see Tables 1–4) belong to the carbonate platforms of Tertiary sequence (in our case middle Eocene to early Oligocene), offshore of Western India. These limestones are present in the western part of the sequence and they are replaced by shale-carbonate alternations in the eastern direction and mostly shales in some places. The sedimentological analysis shows that these limestone reservoirs are highly heterogeneous, varying from mudstones, wackestones/packstones to grainstones with small amounts of clay minerals. Fractures, vugs, and channels are partially filled with calcite. At places moldic/interwoven porosities are noticed. Stylolites, which locally act as permeability barriers, are also present in the tight limestones (He et al., 2014). The limestone is milky white and the foraminifera wackestone/packstone facies are sometimes sparitized (Sharma et al., 2006). They are from heterogeneous reservoirs (Winn, 1957). The dominant mineralogy of our samples is calcite with some quartz. In few samples, Rai et al. (2004) have found minor amount of clay (illite) as well. The porosity of the core samples ranges from 0.05 to 0.24 and their permeability from 0.026 mD to 34 mD (1 D = 1 Darcy; 1 mD $\approx 10^{-15}$ m^2, see Tables 1–4).

Batch 3 and batch 4 are formed by carbonates rock samples from France. They have been selected to provide samples with larger porosities (up to 0.32) and permeability values (up to 3,000 mD) complementing therefore the data sets from batch 1 and batch 2. They include algal rhodolith packstones called the Estaillades limestones from Provence (southeast of France), limestones from Saint-Emilion (Oligocene, Aquitaine Basin, France), and dolomites (Paleocene, Aquitaine Basin, France). Their properties are reported in

Table 2
Electrical Properties at a Pore Water Conductivity of 0.07 S m^{-1} (NaCl, 22°C) of Batch 1

Sample ID	σ′ (S/m) (1 Hz)	σ′ (S/m) (1 kHz)	M_n (S/m) (1 Hz–1 kHz)	σ″ (S/m) (32 Hz)	F (–)	σ_S (S/m)
I3b	5.22E−04	5.36E−04	1.40E−05	2.66E−06	582	0.00033
I24	9.08E−03	9.16E−03	8.00E−05	6.56E−06	55	0.0065
I51	1.52E−02	1.53E−02	1.00E−04	1.17E−05	107	0.0109
I21	6.83E−03	7.06E−03	2.30E−04	4.51E−05	244	0.0048
I42b	1.27E−02	1.28E−02	1.00E−04	4.37E−06	60	0.0103
I42a	4.15E−03	4.16E−03	1.00E−05	9.76E−07	204	0.0033
I18	6.51E−02	6.92E−02	4.10E−03	9.37E−04	38	0.0411
I39	1.26E−03	1.28E−03	2.00E−05	3.82E−06	625	0.0008
I23	3.84E−03	3.93E−03	9.00E−05	2.04E−05	334	0.0024
I15	1.03E−02	1.08E−02	5.00E−04	1.12E−04	283	0.0082
I19	7.81E−03	8.22E−03	4.10E−04	9.23E−05	172	0.0058
I48	3.5E−03	3.61E−03	3.00E−05	4.43E−06	84	0.0023

The normalized chargeability is determined as M_n(1 Hz–1 kHz) = σ′(1 kHz)−σ′(1 Hz). The parameter F denotes the formation factor and σ_S denotes the surface conductivity (S/m) of the core samples. This surface conductivity corresponds to the last term of Equation (3).

Tables 5–8. The samples of batch 5 (see Tables 9 and 10) have the same origin than the samples of batches 1 and 2 but were measured later in time.

3.2. Measurements

The porosity of the core samples was measured by measuring the weight of the core samples (dry and water saturated) and their volume. The specific surface area was measured with the BET technique (Brunauer et al., 1938). The term BET stands from the names of Brunauer, Emmett and Teller, who have developed a nitrogen sorption method working on dry powders to determine their specific surface areas. Another fundamental parameter to characterize the electrochemical reactivity of the mineral surface is the CEC, which stands for cation exchange capacity. The CEC corresponds, at a given pH and concentration of the potential-determining ions, to the number of exchangeable sites on the surface of a given mineral. It is measured through a titration experiment and normalized by the dry mass of minerals. The CEC of the core samples from batch 4 were determined with the cobalt hexamine method (Aran et al., 2008) and transformed into specific surface area with a surface charge density (see Figure 3) Q_S = 0.08 C m^{-2}. Lee et al. (2016) obtained an effective charge density of 0.02 C m^{-2} using Rb^+ sorption on calcite (104) using X-ray reflectivity.

Table 3
Petrophysical Properties of the Core Samples From Batch 2 (12 samples)

Sample ID	Description	Porosity ϕ (–)	S_{sp} (BET) (m^2/g)	k (m^2)
I2	Limestone	0.067	–	0.16E−15
I3a	Limestone	0.040	14.256	0.0295E−15
I38b	Limestone	0.10	17.434	1.12E−15
I8	Wackestone	0.08	10.206	0.34E−15
I6	Wackestone	0.15	–	4.71E−15
I45	Limestone	0.15	23.436	3.39E−15
I47	Limestone	0.16	16.641	1.81E−15
I43	Limestone	0.21	21.781	32.45E−15
I49	Micrite	0.24	280.786	26.7E−15
I32	Limestone	0.11	–	0.19E−15
I34	Limestone	0.13	15.395	0.77E−15
I5	Wackestone	0.051	–	0.028E−15

Abbreviations: BET, Brunauer, Emmett and Teller.
The quantity k denotes the water permeability measured with a permeameter.

Frequency domain induced polarization measurements were performed on the 57 core samples over the frequency range from 100 mHz to 45 kHz using the ZELSIP04-V02 impedance meter (Zimmermann et al., 2008). The protocol used for the measurements is the same as the one reported by Revil et al. (2017a) and will not be discussed further here. The equipment and sample holder are shown in Figures 4a and 4b. Non-polarizable Ag/AgCl medical electrodes are used for both the current injection (electrodes A and B) and the potential electrodes M and N. Some spectra are shown in Figures 4c and 5. From Figure 4c, it is clear that below 100 Hz, the response is dominated by the induced polarization component rather than by the Maxwell-Wagner polarization.

Table 4
Electrical Properties at at a Pore Water Conductivity of 0.07 S m^{-1} (NaCl, 25°C) of Batch 2

Sample ID	σ′ (S/m) (1 Hz)	σ′ (S/m) (1 kHz)	M_n (S/m) (1 Hz–1 kHz)	σ″ (S/m) (32 Hz)	F (–)	σ_S (S/m)
I2	2.43E−03	2.63E−03	2.00E−04	8.77E−06	476	0.0019
I3a	6.16E−03	6.47E−03	3.10E−04	7.11E−05	617	0.0011
I38b	3.17E−03	3.20E−03	3.00E−05	4.05E−06	221	0.0029
I8	8.78E−03	9.23E−03	4.50E−04	0.0001	85	0.0076
I6	7.34E−03	7.97E−03	6.30E−04	1.36E−04	52	0.0061
I45	5.08E−03	5.22E−03	1.40E−04	2.47E−05	46	0.0035
I47	4.27E−03	4.33E−03	6.00E−05	2.99E−06	72	0.0029
I43	8.00E−03	8.28E−03	2.80E−04	6.74E−06	38	0.0060
I49	1.14E−02	1.16E−02	2.00E−04	1.42E−05	41	0.0080
I32	7.84E−04	7.96E−04	1.20E−05	2.2E−06	185	0.00019
I34	1.54E−03	1.57E−03	3.00E−05	5.86E−06	163	0.0026
I5	1.85E−03	1.89E−03	4.00E−05	8.69E−06	1,049	0.00044

The normalized chargeability is determined as M_n(1 Hz–1 kHz) = σ′(1 kHz)−σ′(1 Hz). The parameter F denotes the formation factor and σ_S denotes the surface conductivity (S/m) of the core samples.

The measurements for batches 1, 3, and 5 were done at three different salinities with an initial saturation made with tap water. The first saturation was performed under vacuum using dry samples. The initial conductivity of the tap water was 0.029 S m^{-1}. We waited one month before doing the induced polarization measurements. After one month, the conductivity of the water in the becker in equilibrium with the core sample was 0.079 S m^{-1}. The next salinities were imposed by diffusion with NaCl brines. The second initial conductivity was 0.50 S m^{-1}. After one month, the conductivity in equilibrium with the sample was 0.58 S m^{-1}. For the third salinity, the initial pore water conductivity was 5 S m^{-1} and after a month, the final conductivity was the same (5 S m^{-1}). For the last salinity, the initial pore water conductivity was 10 S m^{-1}. After one month, the final conductivity was 9.18 S m^{-1}. The three salinities used for the last solutions were 2.6 g L^{-1}, 37 g L^{-1}, and 73.1 g L^{-1}, respectively. The same protocol was used for batch 4 but three other pore water conductivities corresponding to 0.051, 5.0, and 13.0 S m^{-1} (NaCl, 25°C) were used. The pH of the solution was measured and found to be 8.4 ± 0.1.

Table 5
Petrophysical Properties of the Core Samples From Batch 3 (12 samples)

Sample ID	Description	Porosity ϕ (–)	S_{sp} (BET) (m^2/g)	k (m^2)
F1	Limestone-REP	0.15	0.34	46.2E−15
F2	Limestone-RFF	0.32	1.41	22.8E−15
F3	Limestone	0.26	0.004	1061E−15
F4	Dolomite	0.26	–	–
F5	Dolomite	0.24	–	–
F6	Limestone	0.25	–	–
F7	Limestone	0.28	0.18	259E−15
F8	Limestone	0.27	–	–
F9	Limestone-Estallade	0.24	2.13	1044E−15
F10	Limestone-Brauvilliers	0.28	1.54	7.9E−14
F11	Limestone	0.26	–	–
F12	Limestone- Saint Emilion	0.25	1.33	2987E−15

Abbreviations: BET, Brunauer, Emmett and Teller.
The specific surface areas have been measured using the BET technique. The quantity k denotes the water permeability measured with a permeameter.

4. Results

4.1. Archie's Law and Surface Conductivity

The in-phase conductivity (at a frequency of 1 Hz) is reported as a function of the pore water conductivity in Figure 6. We see that the data are reasonably fitted by a linear relationship between the two parameters (see Equations 3 and 4). These linear trends are used to determine in a log-log space the intrinsic formation factor $F = \phi^{-m}$ and the surface conductivity $\sigma_S = \phi^{m-1}\rho_g BQ_S\, S_{Sp}$ (noticing that the high-frequency and low-frequency surface conductivity are close to each other). The values of these parameters are reported in Tables 1–8. Our study is showing that surface conductivity cannot be ignored in our carbonate rocks. This is in contrast with the general assumption made so far that surface conductivity can be always safely ignored in carbonates (e.g., Regnet et al., 2019 and references therein), which may obviously lead to incorrect estimates of the value of the formation factors. The values of the fundamental parameters

Table 6
Electrical Properties at a Pore Water Conductivity of 0.07 S m^{-1} (NaCl, 22°C) of Batch 3

Sample ID	σ′ (S/m) (1 Hz)	σ′ (S/m) (1 kHz)	M_n (S/m) (1 Hz–1 kHz)	σ″ (S/m) (32 Hz)	F (−)	σ_S (S/m)
F1	2.38E−02	2.45E−02	7.00E−04	8.90E−05	40	0.023
F2	7.25E−02	7.33E−02	8.00E−04	1.60E−04	18	0.051
F3	2.29E−02	2.30E−02	1.00E−04	5.76E−06	23	0.020
F4	6.09E−02	6.28E−02	1.90E−03	3.94E−04	19	0.042
F5	3.55E−02	3.57E−02	2.00E−03	6.59E−05	36	0.024
F6	5.94E−02	5.97E−02	3.00E−04	9.51E−05	25	0.036
F7	7.26E−02	7.32E−02	6.00E−04	9.07E−05	16	0.068
F8	7.91E−02	7.94E−02	3.00E−04	6.03E−05	17	0.074
F9	5.56E−02	5.58E−02	2.00E−04	4.86E−05	18	0.052
F10	6.67E−02	6.71E−02	4.00E−04	4.22E−05	16	0.062
F11	2.83E−02	2.86E−02	3.00E−04	4.88E−05	21	0.025
F12	7.76E−02	7.88E−02	1.20E−03	3.20E−04	28	0.074

The (partial) normalized chargeability is determined as M_n(1 Hz–1 kHz) = σ′(1 kHz)−σ′(1 Hz). The parameter F denotes the formation factor and σ_S denotes the surface conductivity (S/m) of the core samples.

entering our model will be reported in Table 11. We know that our core samples are reported to include some clay minerals. While we cannot prove here this point, we suggest that part of the observed surface conductivity may be due to the presence of these clay minerals and the existence of a structural charge in the carbonate-type minerals.

The formation factors are plotted as a function of the porosity in Figure 7. We see that the two parameters are highly correlated to each other through a power-law relationship known as Archie's law $F = \phi^{-m}$ (Archie, 1942) with a cementation exponent m of 2.14 ± 0.03 for our data set (Table 11). The high correlation coefficient observed in Figure 7 ($r^2 = 0.75$) is a remarkable feature in itself. This should point out that this value of the cementation (porosity) exponent is valid for unfractured carbonate rocks. Focke and Munn (1987) show that the cementation exponent m of sucrosic dolomites with intercrystalline porosity (in the porosity range 0.05–0.32) and carbonates with chalky porosity (in the same porosity range) is in the range 1.9–2.2. For carbonates with abundant vugs, the value of the cementation exponent increases is higher than 2 while the presence of micro-cracks tends to reduce the value of m below 2 (Kazatchenko & Mousatov, 2002). A warning is also needed here. There is indeed a huge literature regarding the value of the cementation exponent of carbonate rocks. That said, since a lot of published works do not consider the

Table 7
Petrophysical Properties of the Core Samples From Batch 4 (6 Samples)

Sample ID	Description	Porosity ϕ (−)	CEC (meq/100 g)	S_{sp} (BET) (m^2/g)	k (m^2)
4–1	Carbonate-rich Clay	0.30	9.0	170	–
4–2	Limestone	0.20	0.97	19	800E−15
4–3	Limestone	0.20	2.69	52	12E−15
4–4	Limestone	0.21	3.58	70	–
4–5	Limestone	0.14	0.32	6	7E−15
4–6	Limestone	0.17	0.10	2	6E−15

Abbreviations: BET, Brunauer, Emmett and Teller; CEC, cation exchange capacity.
CEC (1 meq/100 g = 963.20 C kg^{-1}). The measured CEC are converted to specific surface area measurements using a charge density of 0.5 elementary charges per nm^2 (see discussion in the main text). The quantity k denotes the water permeability measured with a permeameter.

Table 8
Electrical Properties at a Pore Water Conductivity of 0.07 S m^{-1} (NaCl, 25°C) of Batch 4

Sample ID	σ′ (S/m) (1 Hz)	σ′ (S/m) (1 kHz)	M_n (S/m) (1 Hz–1 kHz)	σ″ (S/m) (32 Hz)	F (–)	σ_S (S/m)
4–1	0.12765	0.13520	0.00755	165.0E−5	2.9	0.11
4–2	0.0049881	0.0051036	0.000116	3.20E−5	16	0.0038
4–3	0.0099220	0.010573	0.000651	7.86E−5	26	0.0080
4–4	0.019310	0.019971	0.000661	11.4E−5	23	0.017
4–5	0.0011020	0.0011645	0.0000625	0.88E−5	63	0.00029
4–6	0.0020849	0.0021825	0.0000976	1.25E−5	34	0.00060

The normalized chargeability is determined as M_n(1 Hz–1 kHz) = σ′(1 kHz)−σ′(1 Hz). The parameter F denotes the formation factor and σ_S denotes the surface conductivity (S/m) of the core samples.

possibility of surface conduction, the derived values of the cementation exponents should be considered with caution.

We focus now on the surface conductivity of carbonate rocks, which is an intriguing subject. Fundamentally, we expect some forms of surface (interface) conduction in carbonate rocks since calcite possesses an electrical double layer (e.g., Al Mahrouqi et al., 2017) and because the potential presence of clays in these rocks (documented in the petrological investigations). Surface conductivity is obtained according to the procedure mentioned above and illustrated in Figure 6 like for siliciclastic materials. In Figure 8, we plot the surface conductivity as a function of the specific surface areas divided by the tortuosity of the pore space (product of the formation factor by the connected porosity). As predicted by the theory (last terms of Equations 3 and 4), the surface conductivity is linearly related to this "reduced" specific surface area but with a slope smaller than for clayey sandstones. This slope difference could be expected based on the difference between the surface charge density Q_S of clays (~5 elementary charges per nm^2) and calcite (~0.5 elementary charges per nm^2). Note that these values are given for simple supporting electrolytes (NaCl) at low ionic strengths of the pore water, which is consider in chemical equilibrium with the minerals. Obviously, this charge density is expected to increase with the salinity for both silicates and carbonates (as shown in Figure 5).

Table 9
Petrophysical Properties of the Core Samples From Batch 5 (15 Samples)

Sample ID	Description	Porosity ϕ (–)	S_{sp} (BET) (m^2/g)	k (m^2)
I52	Limestone	0.21	26.868	1.96E−15
I4	Limestone	0.14	–	4.9E−17
I9a	Limestone	0.08	60.417	5.782E−16
I10	Wackestone	0.14	39.802	7.742E−16
I11	Wackestone	0.12	38.769	6.28E−17
I12	Wackestone	0.13	–	–
I13	Wackestone	0.07	–	–
I14	Wackestone	0.08	72.388	5.684E−18
I16	Limestone	0.12	38.682	3.724E−16
I17	Wackestone	0.14	3.454	1.96E−17
I20	Limestone	0.23	52.349	3.92E−15
I22	Limestone	0.07	27.867	4.9E−18
I25	Limestone	0.23	1.991	1.08E−14
I27	Limestone	0.16	64.056	8.33E−16
I36	Limestone	0.08	18.232	1.96E−17

Abbreviations: BET, Brunauer, Emmett and Teller; CEC, cation exchange capacity.
CEC (1 meq/100 g = 963.20 C kg^{-1}). The measured CEC are converted to specific surface area measurements using a charge density of 0.5 elementary charges per nm^2 (see discussion in the main text). The quantity k denotes the water permeability measured with a permeameter.

Using the relationship $\sigma_S^{\infty} = \phi^{m-1}\rho_g B Q_S S_{Sp} \approx \sigma_S^0$ (see Equation 3), we can obtain the value of the mobility of the counterions from the slope of the trend shown in Figure 8. We obtain $B(Na^+, 25°C, \text{calcite}) = 1.0 \times 10^{-8}$ $m^2s^{-1}V^{-1}$ for the carbonate rocks. This value is close to the value of the mobility of sodium in the Stern layer of calcite obtained independently by Leroy et al. (2017) and given by 0.6×10^{-8} $m^2s^{-1}V^{-1}$. Both values are substantially smaller than the value of the mobility of sodium in the bulk pore water ($\beta(Na^+, 25°C) = 5.8 \times 10^{-8}$ $m^2s^{-1}V^{-1}$ at 25°C).

4.2. Normalized Chargeability and Quadrature Conductivity

In Figure 9, we plot the normalized chargeability versus the specific surface area divided by the bulk tortuosity of the pore space. The slope of the trend allows computing the mobility of the counterions for polarization and we obtain $\lambda(Na^+, 25°C, \text{calcite}) \approx 2 \times 10^{-10}$ $m^2s^{-1}V^{-1}$. This value is reported in Table 11.

In Figure 10, we test the predictions of the constant phase model and we obtain a very good match between the model prediction and the data with

Table 10
Electrical Properties at a Pore Water Conductivity of 0.1913 S m^{-1} (NaCl, 25°C) of Batch 5

Sample ID	σ′ (S/m) (1 Hz)	σ′ (S/m) (1 kHz)	M_n (S/m) (1 Hz–1 kHz)	σ″ (S/m) (32 Hz)	F (−)	σ_S (S/m)
I52	9.71E−03	9.87E−03	1.60E−04	3.73E−05	43.5	0.005
I4	6.90E−03	7.31E−03	4.10E−04	7.81E−05	66.7	0.004
I9a	1.781E−03	1.785E−03	4.00E−06	9.08E−07	400	0.001
I10	1.52E−02	1.62E−02	1.00E−03	2.22E−04	62.5	0.011
I11	3.77E−02	3.94E−02	1.70E−03	3.94E−04	66.7	0.03
I12	4.49E−02	4.72E−02	2.30E−03	5.67E−04	58.8	0.04
I13	1.03E−02	1.10E−02	7.00E−04	1.34E−04	192	0.009
I14	1.65E−02	1.76E−02	1.10E−03	2.51E−04	111	0.01
I16	1.03E−02	1.07E−02	4.00E−04	5.91E−05	110	0.01
I17	2.68E−02	2.87E−02	1.90E−03	4.99E−04	76.9	0.02
I20	4.04E−02	4.34E−02	3.00E−03	7.38E−04	19.2	0.03
I22	1.18E−02	1.22E−02	4.00E−04	8.11E−05	303	0.009
I25	9.57E−03	1.06E−02	1.03E−03	6.19E−05	30.3	0.003
I27	6.02E−03	6.04E−03	2.00E−05	9.04E−06	71.42	0.003
I36	3.97E−03	4.01E−03	4.00E−05	3.21E−06	588	0.003

The normalized chargeability is determined as M_n(1 Hz–1 kHz) = σ′(1 kHz)−σ′(1 Hz). The parameter F denotes the formation factor and σ_S denotes the surface conductivity (S/m) of the core samples.

the predicted slope of 4.4 for a partial normalized chargeability determined over three orders of magnitude in the frequency.

4.3. Surface Conduction Versus Polarization

Kulenkampff and Schopper (1988) were the first to predict that surface conduction and polarization could be somehow interconnected. Weller et al. (2013) observed a linear relationship between induced polarization (characterized by quadrature conductivity or normalized chargeability) and surface conductivity for siliciclastic materials (see also Revil et al., 2017b and references therein). Such linear relationship (predicted by the dynamic Stern layer model and not by membrane polarization) is confirmed for carbonate rocks in Figure 11. The ratio between the normalized chargeability and the surface conductivity provides a direct evaluation of the dimensionless number $R \approx 0.02$ (see Table 11), a value smaller than for siliciclastic sediments for which $R \approx 0.10$.

Table 11
Generic Parameters of the Polarization Model Obtained in This Study

Parameter	Name	Value
ρ_g	Grain density (calcite)	2,710 kg m^{-3}
m	Cementation exponent	2.14 ± 0.03
$B(Na^+, 25°C)$	Counterion mobility for conduction	1.0×10^{-8} m^{2}s^{-1}V^{-1}
$\lambda(Na^+, 25°C)$	Counterion mobility for polarization	2.0×10^{-10} m^{2}s^{-1}V^{-1}
$R = \lambda/B$	Dimensionless number	0.02
Q_S	Surface charge density	0.08 C m^{-2}

The value of Q_S given here is for the low salinity range of a pore water in equilibrium with the mineral assemblage (typically in the range 0.08–0.5 S m^{-1} at 25°C). For higher salinities, this surface charge density is expected to increase with the ionic strength of the pore water solution and may change with the composition of the pore water as well. The value of the apparent mobility of the counterions in the Stern layer is similar to that found in Ricci et al (2013).

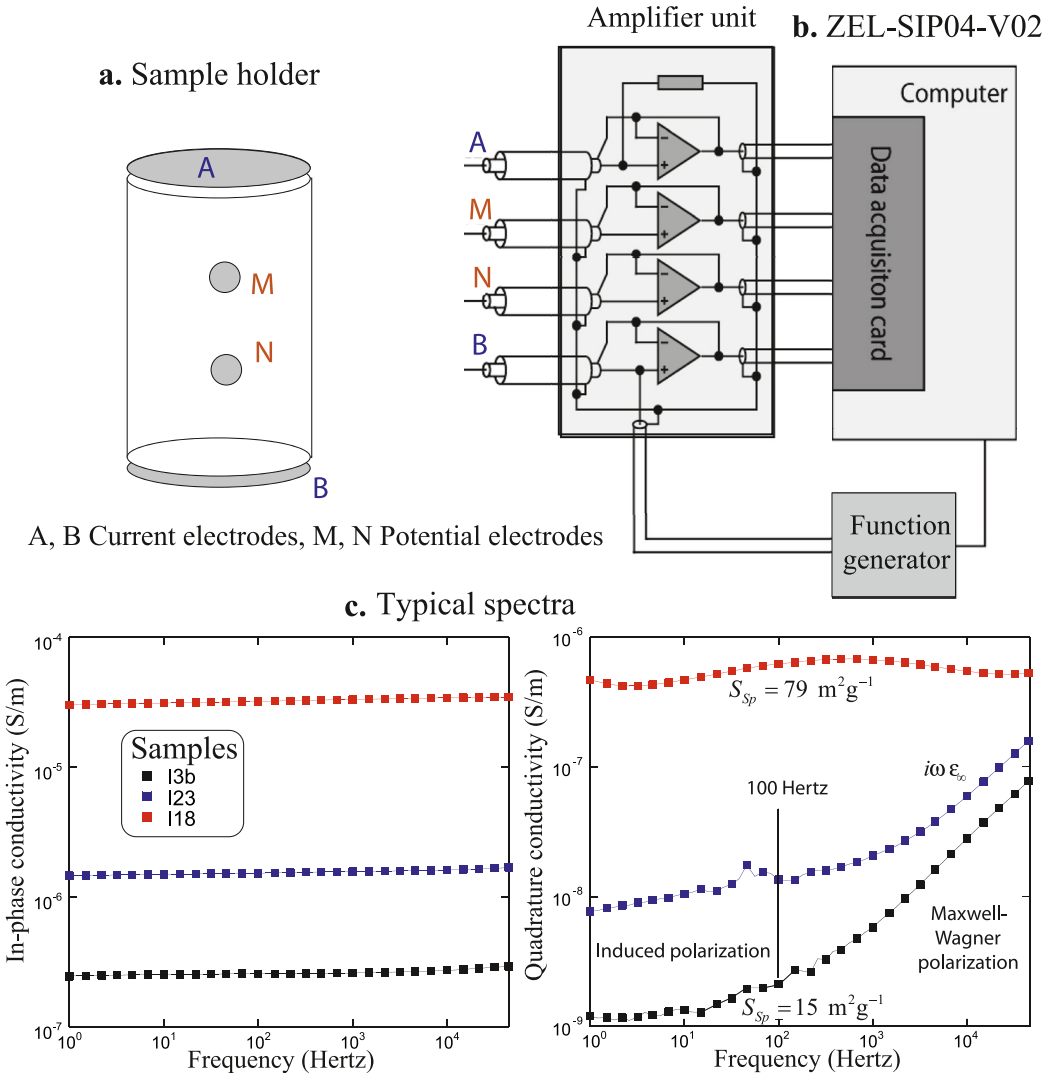

Figure 4. Complex conductivity measurements. (a) Position of the electrodes. (b) Impedance meter developed by Zimmermann et al. (2008). (c) In-phase and quadrature conductivity spectra for three carbonate core samples. The samples are from batch 1. Core sample I18 is characterized by a high specific surface area (79.43 m^2 g^{-1}) while core sample I3b is characterized by a much lower specific surface area (15.45 m^2 g^{-1}).

4.4. Permeability Prediction

In Figure 12, we plot the permeability as the function of the formation factor using the data from Tables 1–8 The permeability values are very well predicted by using just the value of the formation factor with a high correlation factor (r^2 = 0.79 in a log-log plot). Similarly, since the formation factors and the porosities are highly correlated, it is not perhaps surprising that the permeability values are highly correlated to the porosity (see Figures 13 and 14). This means that induced polarization can be used to determine the formation factor (knowing the pore water conductivity) and the specific surface area and then the formation factor can be used to predict the permeability of the carbonate formations. This approach will need to be confirmed by further investigations.

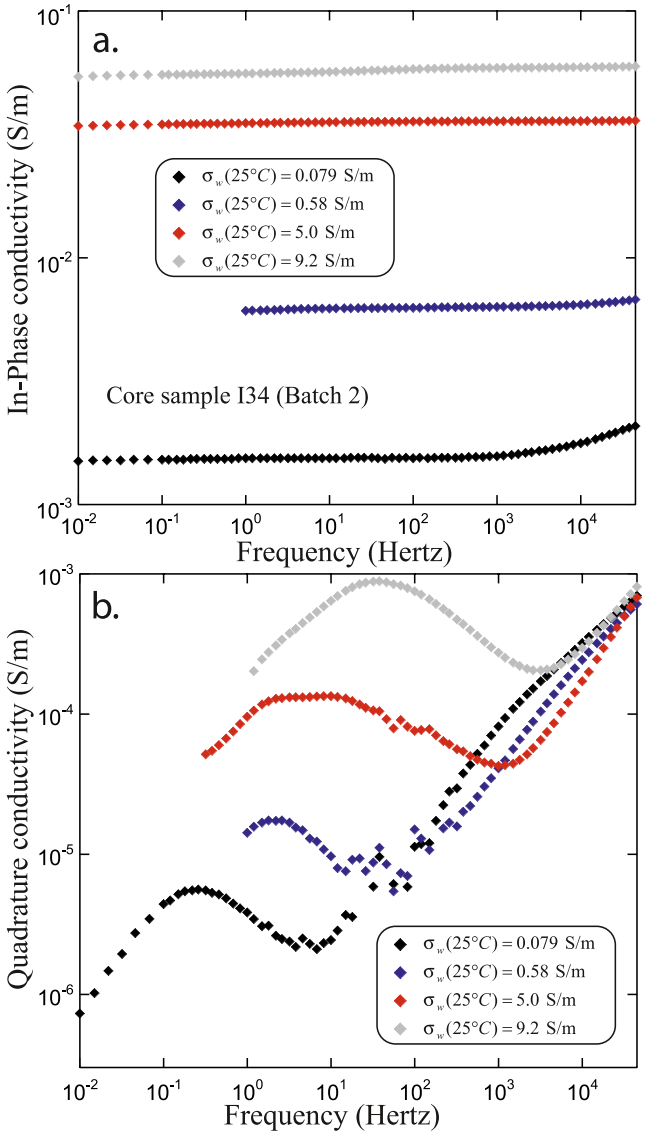

Figure 5. Complex conductivity spectra of Core I34 (batch 2, low specific surface area ~15.4 m^2g^{-1}) for four distinct salinities. (a) In-phase conductivity spectra. (b) Quadrature conductivity spectra.

5. Field Application

5.1. Test Site

Our goal in this section is to apply the previous petrophysical model to a case study in the French Alps over a carbonate formation. We selected as a suitable test site a Mesozoïc limestone formations located in the Bauges (Savoie, subalpine ranges of the Western Alps, see Figure 15). The sedimentary pile is characterized by folding with both synclines and anticlines (Gidon et al., 1970). The Mariet depression corresponds to one of these synclines characterized by a south-north axis and located at an altitude of ~1,000 m above sea level. Its surface area is ~6.5 km^2. Its south expression is limited by the Montagny Fault while its northern portion is bounded by the gorge of the Chéran river.

The whole area is prone to subvertical ground water flow in the underlying karstified limestone where the pore water can be sampled (CDS 73, 1993). The conductivity of the pore water is found to be in the range 0.01–0.05 S m^{-1} (25°C) indicating that the value of the surface charge Q_S inferred from the laboratory data can be used in the field. The Mariet depression has been filled several times by glaciers during the Quaternary (Jaillet et al., 2018). These glaciers have deepen the depression and let behind glacial till infilling composed of allochthonous blocks of various sizes (typically made of granite and gneiss) embedded into a sand-clay matrix. This infilling is overlaid by shallow postglacial peats.

5.2. Data Acquisition

A south-north 1.9 km-long profile was performed with 96 electrodes and a spacing between the electrodes of 20 m and a depth of investigation of ~220 m (Figure 15). In the south and north of the profiles, the limestones outcrops while the central portion of the profile corresponds more or less to the maximum thickness of the glacial till infilling. Data were acquired using a Wenner-α array characterized by equal spacing between the electrodes and the voltage electrodes MN located in between the current electrodes AB. We use a current injection with a period of 1 s. The secondary voltages were acquired over 1.3 s with a dead-time of 0.2 s and over 10 windows of 0.1 s. Two stacks were performed to obtain the standard deviations and the raw data were filtered based on their standard deviations with a threshold of 1%. The data were acquired with an ABEM-Terrameter SAS-4000 resistivity meter. We used 10-mm-diameter and 120-mm-long stainless steel electrodes for the survey. The choice of these electrodes for an induced polarization survey is justified by the study of Labrecque and Daily (2008). The contact resistance between the electrodes and the ground was always below 1 kohm and the injected current was typically of 200 mA. Topography along the profile was acquired with a differential GPS with a precision of 10 cm. The profile comprises 96 electrodes and 770 data points were used for the inversion (out of 807). The duration of the injection is 1 s so the data corresponds to a frequency of ~1 Hz, for which we don't have to worry about the Maxwell-Wagner contribution.

The data were inverted with the RES2DINV-3.54.44 software using a smoothness-constrained least squares method and the standard Gauss-Newton method (Loke & Barker, 1996). The inversion was stopped at the fourth iteration when the convergence criterion was reached. The RMS error for conductivity is 10.1 while it is 0.1 for the induced polarization survey.

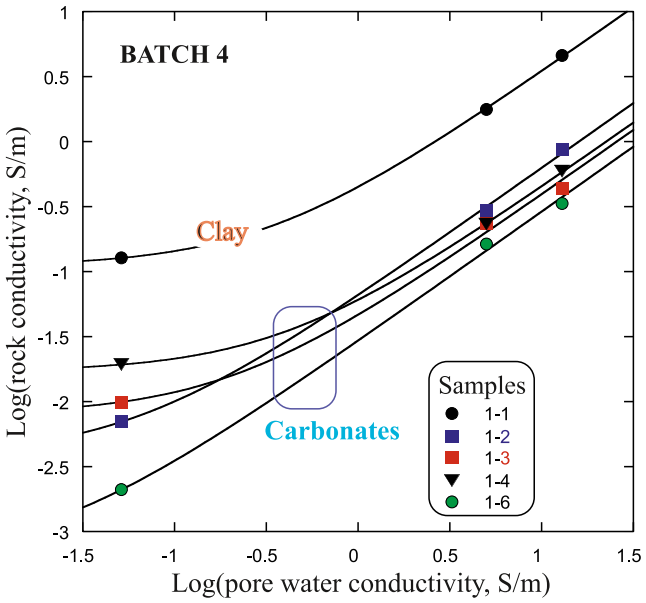

Figure 6. In-phase conductivity versus pore water conductivity. The formation factor and the surface conductivity are determined in a log-log space using a non-linear inversion procedure. The curves correspond to the best fit to determine the formation factor and the surface conductivity.

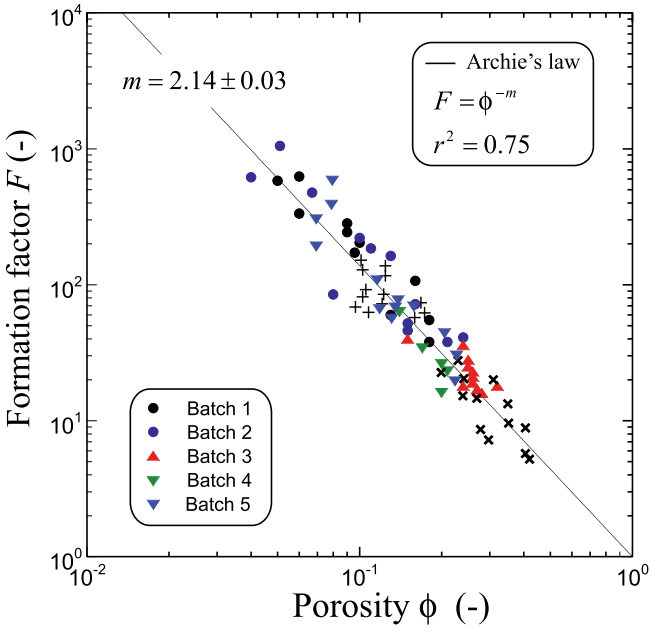

Figure 7. Intrinsic formation factor versus porosity and fit with Archie's law. The clay sample has been removed from the data set because characterized by a higher value of the cementation exponent. The crosses represent the dolomite core samples from Halisch et al. (2014, symbol +) consisting of large crystals with some dissolution structures (with more than 90% dolomite) and the Aquitaine Danian dolomite core samples investigated by Cerepi (2004, symbol ×).

5.3. Results and Interpretation

The tomogram of the conductivity and normalized chargeability was shown in Figure 16. The normalized chargeability tomogram is reliable thanks to the great quality of the apparent chargeability decay curves (Figure 17). Thanks to the geophysical profile, the maximum depth of the glacial till infilling is estimated to be ~50–60 m. It is characterized by high values of the conductivity and normalized chargeability ($\sigma > 10^{-3}$ S m^{-1}, $M_n > 10^{-5.5}$ S m^{-1}). The underlying limestones are characterized by lower conductivity and normalized chargeability values. Once these tomograms have been obtained, we can use Equations 3 and 5 to express the instantaneous conductivity as a function of the normalized chargeability

$$\sigma_\infty = \phi^m \sigma_w + \frac{M_n}{R} \tag{7}$$

So knowing the value of the pore water conductivity σ_w, the formation factor F, the porosity ϕ, and the specific surface area S_{Sp} can be obtained using the following relationships respectively.

$$F = \sigma_w \left(\sigma_\infty - \frac{M_n}{R} \right)^{-1} \tag{8}$$

$$\phi = F^{-1/m} \tag{9}$$

$$S_{Sp} = \frac{M_n}{\phi^{m-1} \rho_g \lambda Q_S} \tag{10}$$

Equations 8–10 can be used with the value of the parameters in Table 11 and the knowledge of the pore water conductivity.

The formation factor tomogram is shown in Figure 18 and the porosity and specific surface area are shown in Figure 19. We get reasonable values of the porosity and specific surface area showing very clearly the infilling of the Mariet depression. A cross-plot of the normalized chargeability versus the conductivity is shown in Figure 20. This cross-plot indicates that we are below the line corresponding to $M_n = R\sigma_\infty$, indicating that surface conductivity is important but not dominant at this site.

6. Conclusions

Complex conductivity spectra of 57 core samples were measured in a broad frequency range and at four salinities in the laboratory. As far as we know, this works represents the first attempt to apply the dynamic Stern layer concept to understand the induced polarization properties of such broad set of carbonate core samples. The results conform to the predictions of the dynamic Stern layer model and the comparison between the predicted relationships and the experimental data are used to determine the mobility of the counterions entering the model for both conduction and polarization. Because of the presence of clay minerals in some carbonates plus the existence of an electrical double layer on the surface of calcite and dolomite, surface conductivity is not necessarily negligible in carbonate rocks. Our results show that surface conductivity is actually pretty important and should be accounted for in explaining the conductivity of these materials.

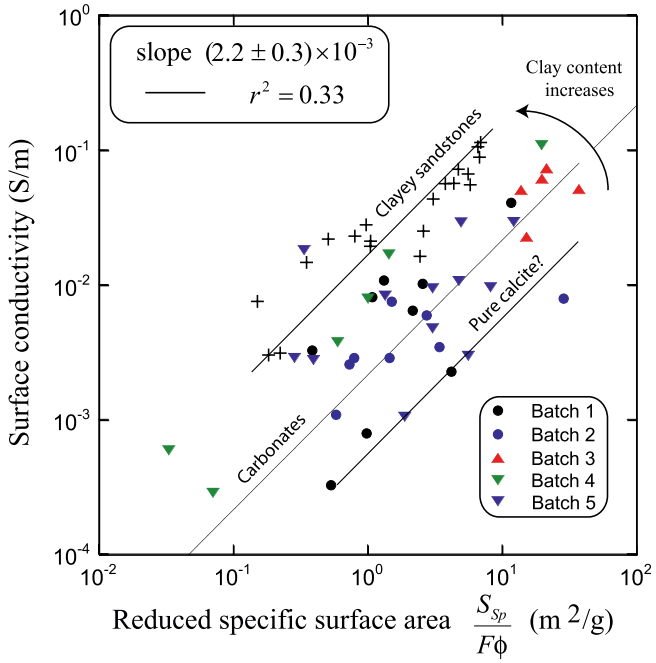

Figure 8. Surface conductivity of carbonate rocks versus reduced specific surface area. The slope of the trend is used to compute the mobility of the counterions. We obtain an apparent mobility for surface conduction by the counterions given by $B = 1.0 \times 10^{-8}$ m^{2}s^{-1}V^{-1}. The tight sandstone data are from Revil et al. (2018). The increase in the clay content of the material is responsible for an increase in the effective surface charge density Q_S, which is intrinsically higher for the surface of clays than for the surface of carbonates.

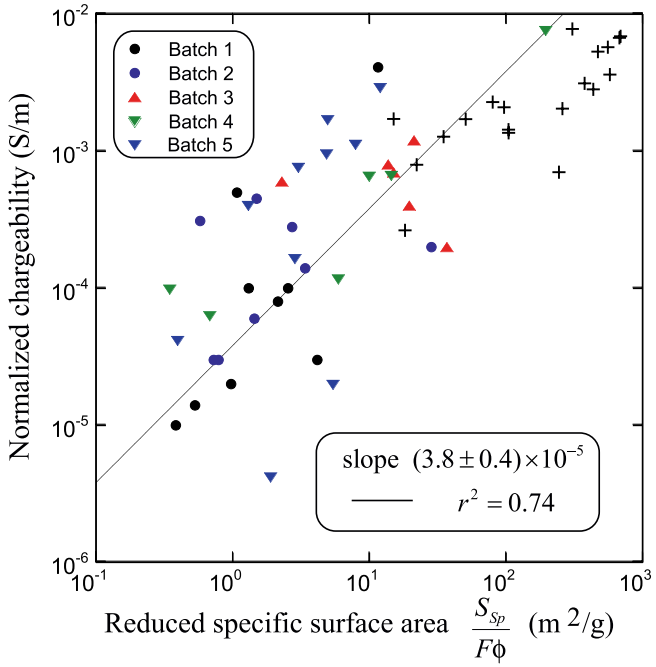

Figure 9. Normalized chargeability versus reduced specific surface area. The slope of the trend is used to compute the mobility of the counterions for polarization. We obtain $\lambda \approx 2 \times 10^{-10}$ m^{2}s^{-1}V^{-1}. The tight sandstone data (marked with crosses, +) are from Revil et al. (2018).

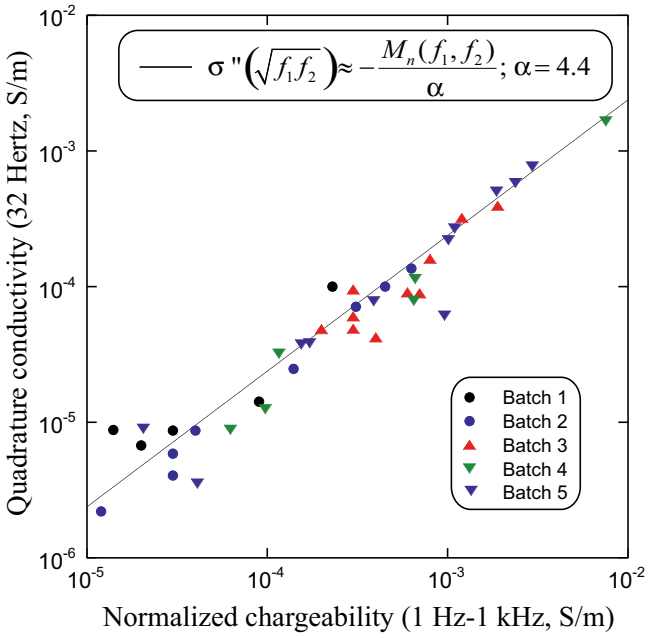

Figure 10. Quadrature conductivity versus (partial) normalized chargeability. The relationship between the two parameters is well-explained by the constant phase model predictions.

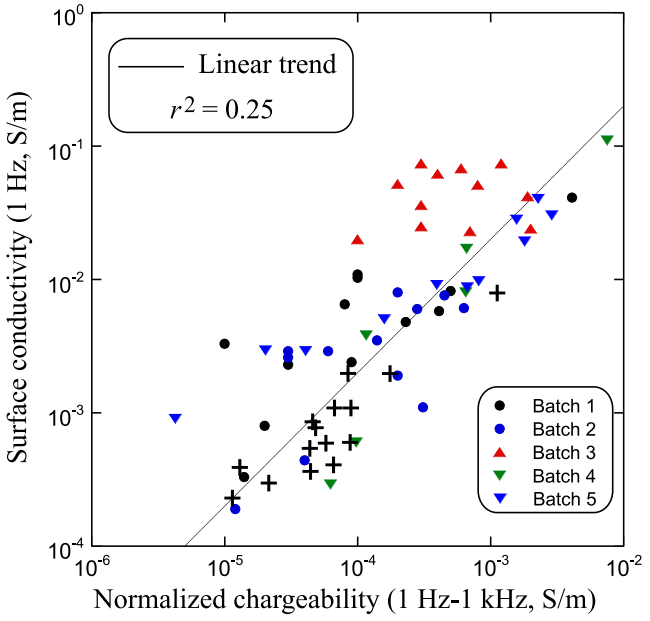

Figure 11. Surface conductivity versus (partial) normalized chargeability. The crosses correspond to the Tushka clay-rich carbonates from Egypt (Halisch et al., 2014). For these carbonates, the quadrature conductivity was transformed into partial normalized chargeability for the frequency range 1 Hz–1 kHz using $\alpha = 4.4$.

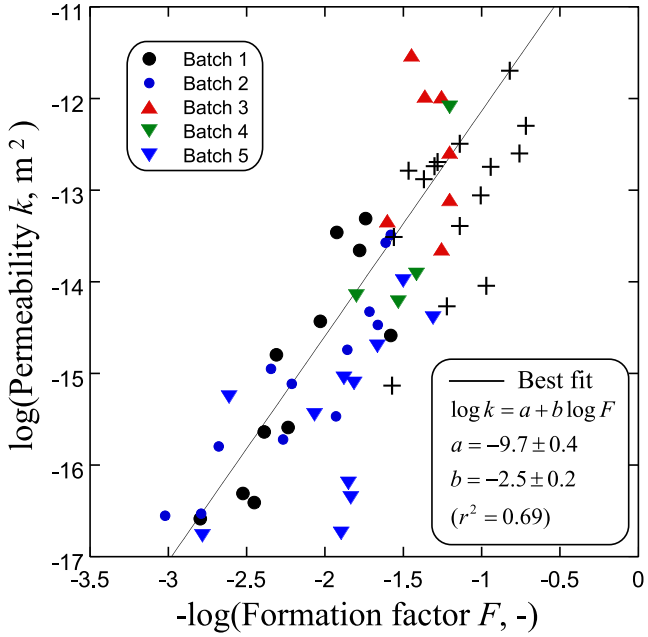

Figure 12. Permeability versus formation factor for all the samples from batches 1 to 5. Surprisingly, we observe that the formation factor alone is a very good indicator of the permeability of the carbonate rocks used in this study. The crosses correspond to the Aquitaine Danian dolomite investigated by Cerepi (2004).

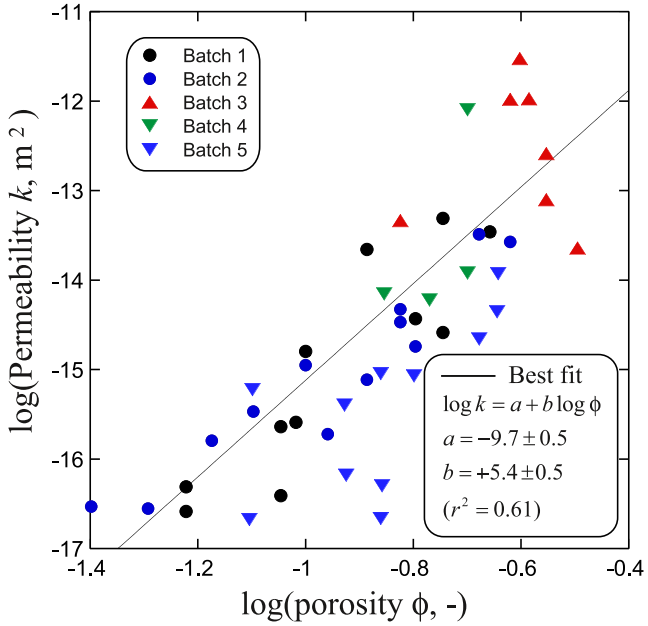

Figure 13. Permeability versus porosity for all the samples from batches 1 to 5. We observe that the formation factor alone is a very good indicator of the permeability of the carbonate rocks used in this study.

Induced polarization can be used to separate the bulk and surface conductivity contributions. Knowing the pore water conductivity, induced polarization can be used to determine the formation factor, which in turn can be used to compute the permeability. The amount of polarization in carbonate rocks is appreciable but the maximum chargeability that can be reached ($R = 0.02$) remains smaller than for clayey siliciclastic rocks ($R = 0.10$). We performed an induced polarization field survey in an area characterized by glacial till infilling overlying a limestone syncline. The field survey is used to image the formation factor, the porosity, and the specific surface area distributions of the formations.

Several key questions remain to be considered in the future including (a) what is the relationship between the relaxation times and the pore size distributions seen from nuclear magnetic resonance or mercury porosimetry? (b) What are the effect of oil saturation and wettability for oil reservoirs and especially the effect of mixed wettability? The first question is important because induced polarization can also be used to provide a tomography of relaxation times, which in turn can be combined with the tomography of the formation factor to determine the permeability distribution of the subsurface. The second question is important to apply induced polarization to oil reservoir monitoring (including large scale controlled source electromagnetic methods, see Wan et al., 2019) and contaminant plumes for which the wettability of the oil is expected to change over time due to the formation of biopolymers associated with bacterial activity.

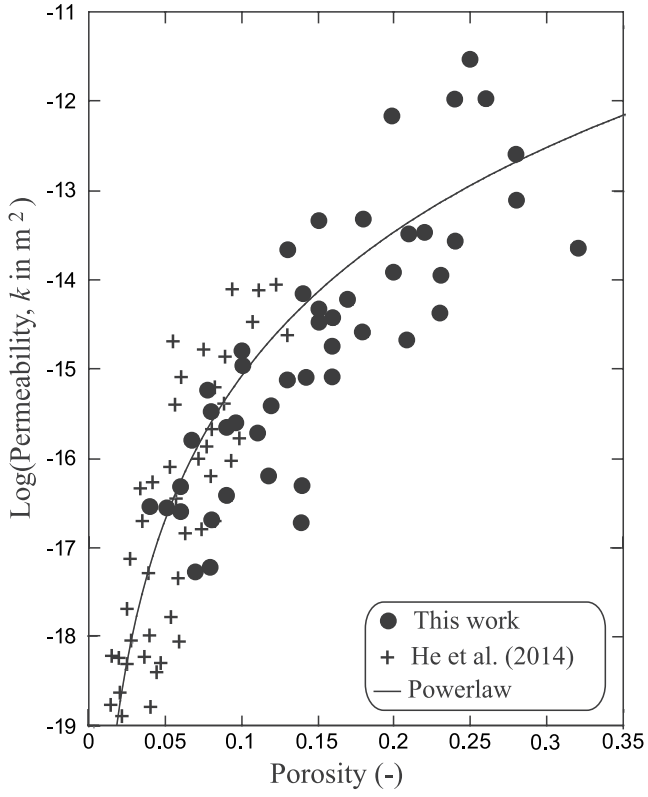

Figure 14. Permeability versus porosity for all the samples from the present study and the work of He et al. (2014, their Figure 10, unfractured carbonate rock samples).

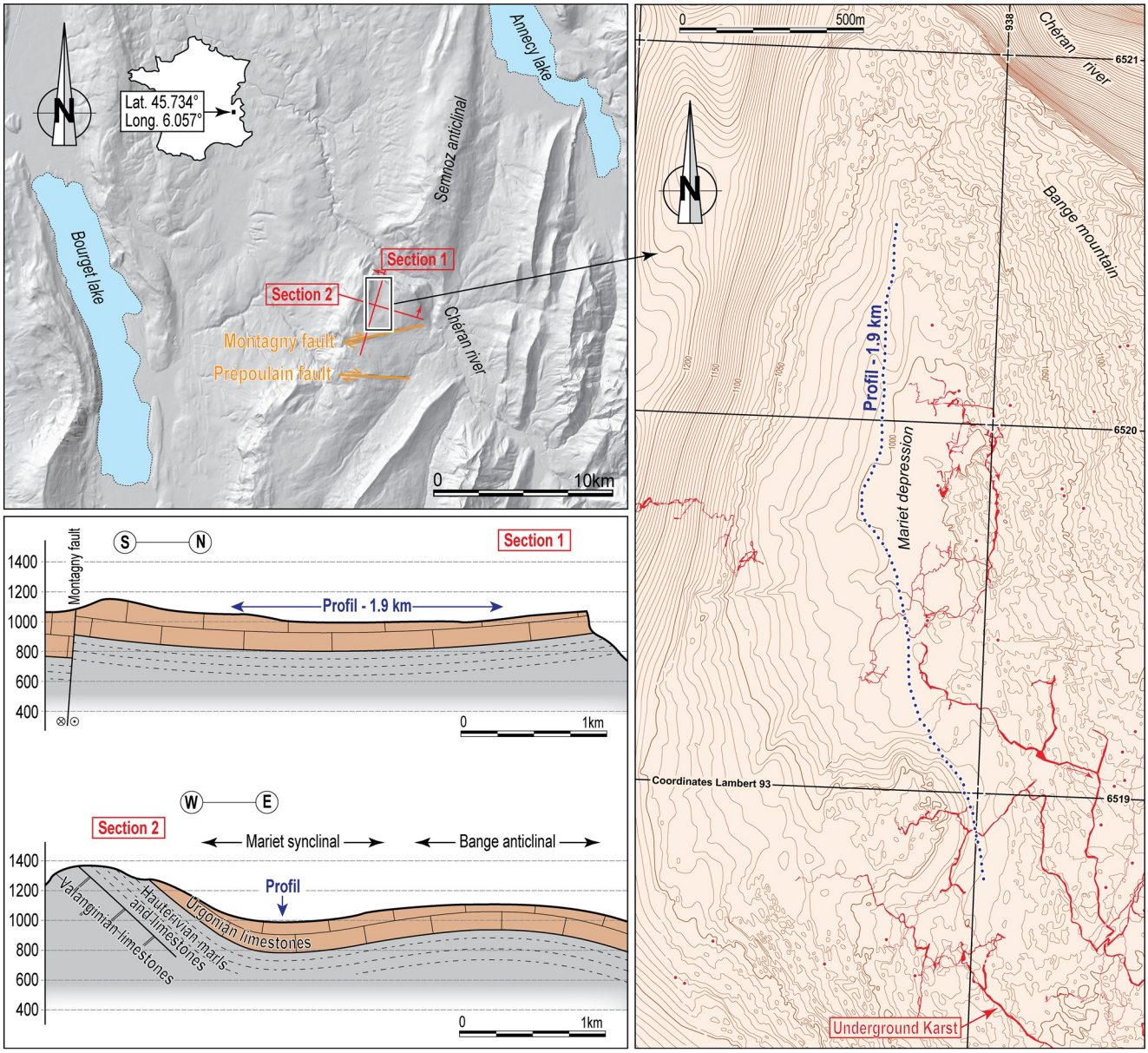

Figure 15. Location of the 1.9 km profile performed along the axis of the Mariet synclinal (Bauges, France). This glacio-karstic depression is typical of those found in the subalpine ranges of the Western portion of the Alps. The syncline is heavily karstified and has been filled several times by glaciers during the cold periods of the Quaternary. The known karstic network is shown in the right-hand side figure.

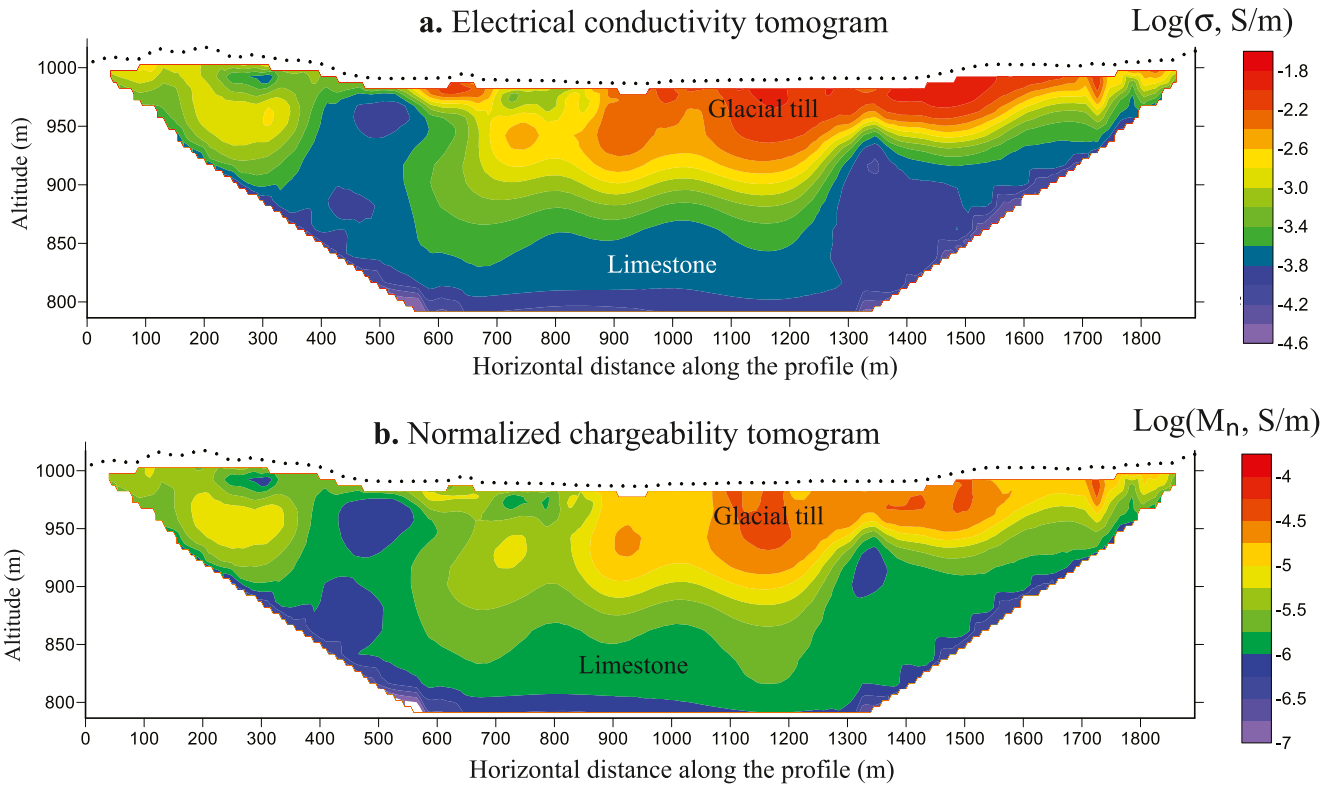

Figure 16. Electrical conductivity and normalized chargeability tomograms along a south-north trend (south is on the left) crossing the Mariet depression. The glacial till infilling is marked by high values of the conductivity and normalized chargeability while the underlying limestone syncline is more resistive and less chargeable.

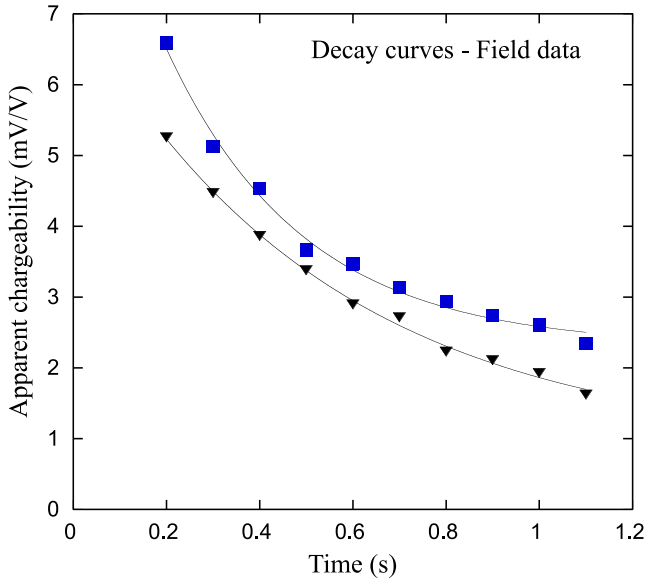

Figure 17. Typical decay curves of the apparent chargeability over time. The current field data set is characterized by a very high quality of the whole set of decay curves. The plain lines correspond to a fit of the data with an exponential decay.

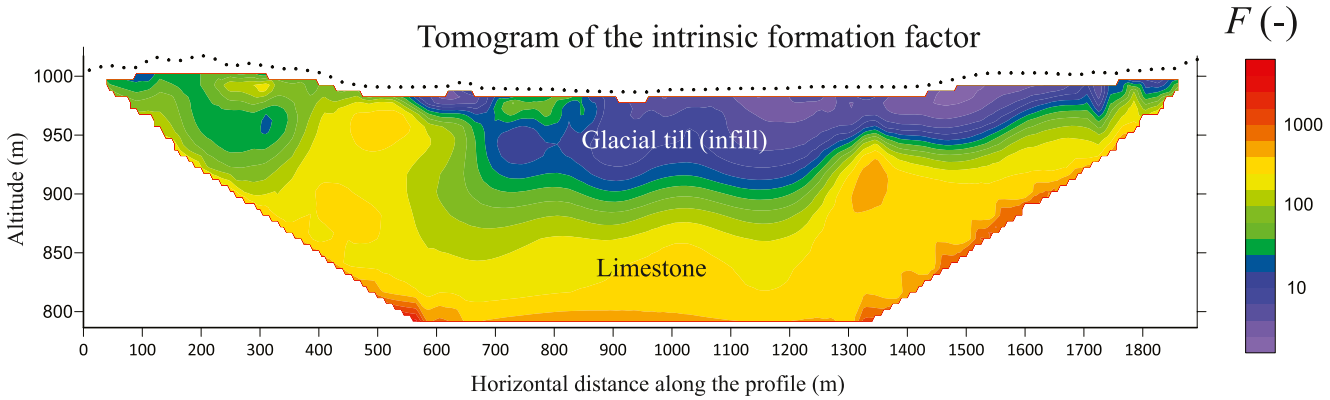

Figure 18. Formation factor tomogram along the south-north profile (south is on the left) crossing the Mariet depression. The glacial till infilling is marked by low values of the formation factor (~10) while the underlying limestone syncline is characterized by high values of the formation factor (>50 up to ~1,000).

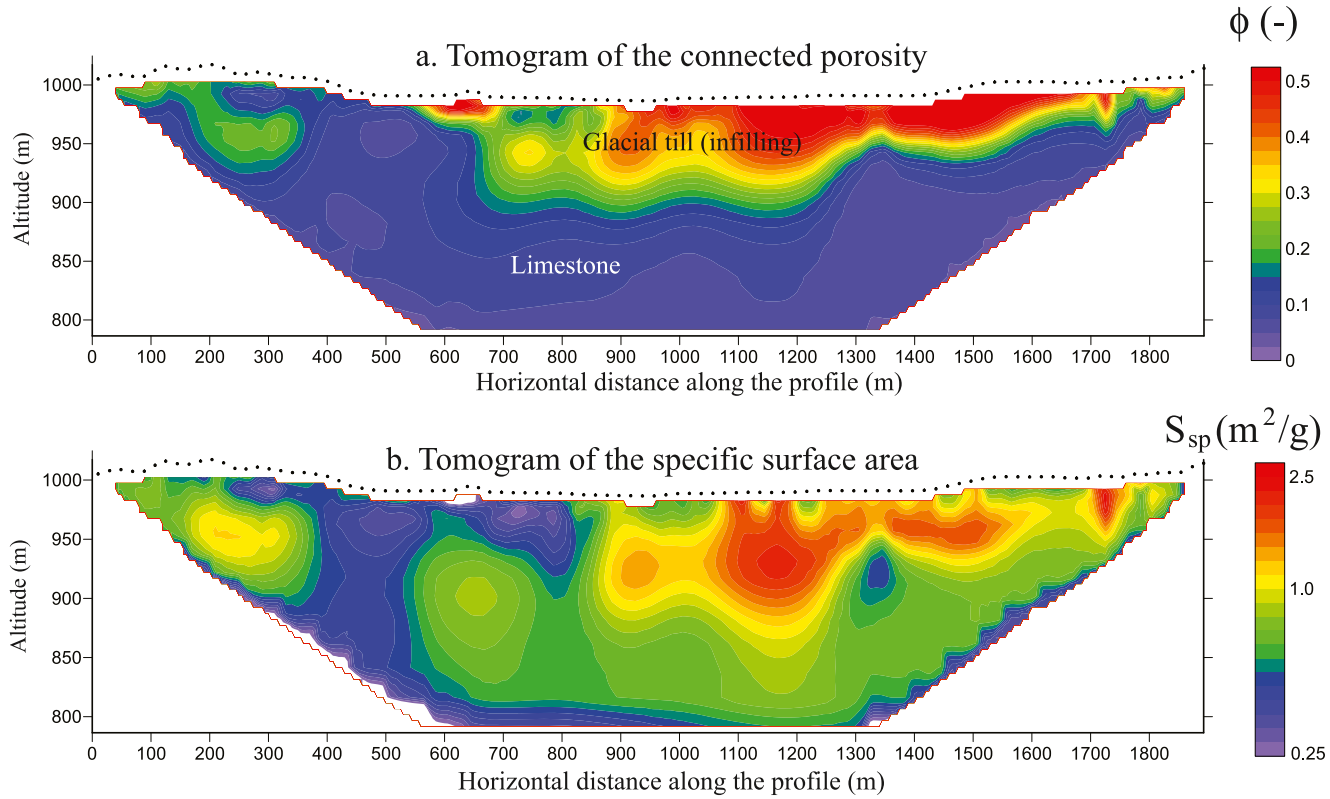

Figure 19. Tomograms of the physical properties along the south-north profile (south is on the left) crossing the Mariet depression. (a) Porosity. The glacial till infilling is very porous (30%–50% porosity) while the limestones are in average characterized by low porosities (around 10%). (b) Specific surface area distribution showing values covering one order in magnitude in variation.

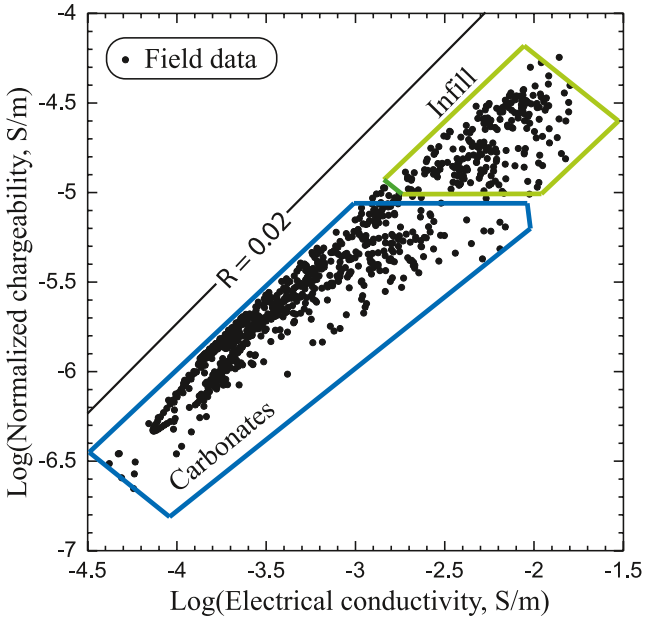

Figure 20. Normalized chargeability versus electrical conductivity. The infill (glacial till) and the limestones are characterized by different values of these two parameters. This plot shows that the surface conductivity of the rocks is important but not dominant since the data are not along the line that would correspond to $R = 0.02$.

Data Availability Statement

Data are published with DRYAD (https://doi.org/10.5061/dryad.sf7m0cg5s).

Acknowledgments

Batches 1, 2, and 5 were provided by the Oil and Natural Gas Corporation Ltd. in India and we thank and acknowledge the support of the overseas visiting doctoral fellowship program by the Department of Science and Technology, Government of India for the financial award to support this work. Batch 3 was provided by the Institut Français du Pétrole-Energies Nouvelles in France. Batch 4 was collected in collaboration with Electricité de France in Provence, France and we thank Sharon Borglin from Lawrence Berkeley National Laboratory for her help with the permeability measurements of batch 3. Regarding the field survey, we thank I-RISK (Research, Development and Innovation platform), the region Auvergne Rhône Alpes (France), and the European FEDER fund for their contribution to the field equipment. We thank the Associate Editor and the two referees for their constructive comments.

References

Abdulsamad, F., Revil, A., Ghorbani, A., Toy, V., Kirilova, M., Coperey, A., et al. (2019). Complex conductivity of graphitic schists and sandstones. *Journal of Geophysical Research*, *124*, 8223–8249. https://doi.org/10.1029/2019jb017628

Al Mahrouqi, D., Vinogradov, J., & Jackson, M. D. (2017). Zeta potential of artificial and natural calcite in aqueous solution. *Advances in Colloid and Interface Science*, *240*, 60–76. https://doi.org/10.1016/j.cis.2016.12.006

Aran, D., Maul, A., & Masfaraud, J. F. (2008). A spectrophotometric measurement of soil cation exchange capacity based on cobaltihexamine chloride absorbance. *Comptes Rendus Geoscience*, *340*(12), 865–871. https://doi.org/10.1016/j.crte.2008.07.015

Archie, G. (1942). The electrical resistivity log as an aid in determining some reservoir characteristics. *Transactions of the AIME*, *146*, 54–62. https://doi.org/10.2118/942054-g

Binley, A., Hubbard, S. S., Huisman, J. A., Revil, A., Robinson, D. A., Singha, K., & Slater, L. D. (2015). The emergence of hydrogeophysics for improved understanding of subsurface processes over multiple scales. *Water Resources Research*, *51*, 3837–3866. https://doi.org/10.1002/2015WR017016

Binley, A., & Kemna, A. (2005). DC resistivity and induced polarization methods. In Y. Rubin, & S. S. Hubbard (Eds.), Hydrogeophysics (pp. 129–156). Springer.

Börner, F. D. (1992). Complex conductivity measurements of reservoir properties, Proceedings of the Third European Core Analysis Symposium, Paris, 359–386.

Brigaud, B., Vincent, B., Carpentier, C., Robin, C., Guillocheau, F., Yven, B., & Huret, E. (2014). Growth and demise of the Jurassic carbonate platform in the intracratonic Paris Basin (France): Interplay of climate change, eustasy and tectonics. *Marine and Petroleum Geology*, *53*, 3–29. https://doi.org/10.1016/j.marpetgeo.2013.09.008

Brunauer, S., Emmett, P. H., & Teller, E. (1938). Adsorption of gasses in multimolecular layers. *Journal of the American Chemical Society*, *60*(2), 309–319. https://doi.org/10.1021/ja01269a023

CDS 73. (1993). L'aventure souterraine en Savoie. Comité départemental de Spéléologie de la Savoie. Editions Gap, coll. Aventure, 304 pp.

Cerepi, A. (2004). Geological control of electrical behavior and prediction key of transport properties in sedimentary porous systems. *Colloids and Surfaces A: Physicochemical and Engineering Aspects*, *241*, 281–298. https://doi.org/10.1016/j.colsurfa.2004.04.049

de Lima, O. A. L., & Sharma, M. M. (1992). A generalized Maxwell-Wagner theory for membrane polarization in shaly sands. *Geophysics*, *57*, 431–440. https://doi.org/10.1190/1.1443257

Flores Orozco, A., Biicker, M., Steiner, M., & Malet, J. P. (2018). Complex-conductivity imaging for the understanding of landslide architecture. *Engineering Geology*, *243*, 241–252. https://doi.org/10.1016/j.enggeo.2018.07.009

Flores-Orozco, A., Gallist, J., Steiner, M., Brandstatter, C., & Fellner, J. (2020). Mapping biogeochemically active zones in landfills with induced polarization imaging: The Heferlbach landfill. *Waste Management*, *107*, 121–132. https://doi.org/10.1016/j.wasman.2020.04.001

Flores Orozco, A., Williams, K. H., Long, P. E., Hubbard, S. S., & Kemna, A. (2011). Using complex resistivity imaging to infer biogeochemical processes associated with bioremediation of an uranium-contaminated aquifer. *Journal of Geophysical Research: Biogeosciences*, *116*(G3). https://doi.org/10.1029/2010JC00159110.1029/2010jg001591

Focke, J. W., & Munn, D. (1987). Cementation exponents in Middle Eastern carbonate reservoirs. *SPE Formation Evaluation*, *2*(2), 155–167. https://doi.org/10.2118/13735-pa

Ford, D. C., & Williams, P. W. (2007). *Karst hydrogeology and geomorphology*. Chichester, England. Wiley.

Friedman, S. P. (2005). Soil properties influencing apparent electrical conductivity: A review. *Computers and Electronics in Agriculture*, *46*, 45–70. https://doi.org/10.1016/j.compag.2004.11.001

Garcia-Artigas, R., Himi, M., Revil, A., Urruela, A., Lovera, R., Sendrós, A., et al. (2020). Time-domain induced polarization as a tool to image clogging in treatment wetlands. *Science of the Total Environment*, *724*, 138189. https://doi.org/10.1016/j.scitotenv.2020.138189

Ghorbani, A., Revil, A., Coperey, A., Soueid Ahmed, A., Roque, S., Heap, M. J., et al. (2018). Complex conductivity of volcanic rocks and the geophysical mapping of alteration in volcanoes. *Journal of Volcanology and Geothermal Research*, *357*, 106–127. https://doi.org/10.1016/j.jvolgeores.2018.04.014

Gidon, P., Enay, R., Caillon, M., & Doudoux, B. (1970). Carte géologique de la France, feuille Rumilly (701). Service de la carte géologique de la France, Paris. Notice explicative, 11 pp.

Gouy, G. L. (1910). Sur la constitution de la charge électrique à la surface d'un électrolyte. *Journal de Physique Théorique et Appliquée*, *9*, 457–468. https://doi.org/10.1051/jphystap:019100090045700

Halisch, M., Hupfer, S., Weller, A., Dlugosch, R., & Plumhoff, H.-P. (2018). An experimental setup for the assessment of effects of carbonate rock dissolution on complex electrical conductivity spectra, Paper SCA2018-051 International Symposium of the Society of Core Analysts held in Trondheim, Norway, 27–31 August 2018, 9 pp.

Halisch, M., Weller, A. & Kassab, M. A. (2014). Impedance spectroscopy on carbonates. International Symposium of the Society of Core Analysts, *paper SCA2014-039*.

Heberling, F., Bosbach, D., Eckhardt, J. D., Fischer, U., Glowacky, J., Haist, M., et al. (2014). Reactivity of the calcite-water-interface, from molecular scale processes to geochemical engineering. *Applied Geochemistry*, *45*, 158–190. https://doi.org/10.1016/j.apgeochem.2014.03.006

Heberling, F., Trainor, T. P., Lutzenkirchen, J., Eng, P., Denecke, M. A., & Bosbach, D. (2011). Structure and reactivity of the calcite-water interface. *Journal of Colloid and Interface Science*, *354*, 843–857. https://doi.org/10.1016/j.jcis.2010.10.047

He, L., Zhao, L., Li, J., Ma, J., Lui, R., Wang, S., & Zhao, W. (2014). Complex relationship between porosity and permeability of carbonate reservoirs and its controlling factors: A case study of platform facies in Pre-Caspian Basin. *Petroleum Exploration and Development*, *41*(2), 225–234. https://doi.org/10.1016/s1876-3804(14)60026-4

Hizem, M., Budan, H., Deville, B., Faivre, O., Mosse, L., & Simon, M. (2008). Dielectric Dispersion: A new wireline petrophysical measurement, SPE Annual Technical Conference and Exhibition, 21–24 September, Denver, Colorado, USA SPE-116130-MS. https://doi.org/10.2118/116130-MS

Hupfer, S., Halisch, M., & Weller, A. (2017). Using low frequency electrical impedance spectroscopy for an enhanced pore space characterization and assessment of carbonates. *Proceedings of the International Symposium of the Society of Core Analysts, 27–30 August 2017,*Vienna, Austria, 1–8.

Jaillet, S., Pons-Branchu, E., Hobléa, F., Berthet, J., Deline, P., Duvillard, P. A., & Génuite, K. (2018). La dépression glacio-karstique du Mariet (Bauges occidentales, France): Un marqueur de l'englacement würmien des Alpes françaises du Nord. *Géomorphologie: Relief, Processus, Environnement*, *24*(2), 107–120. https://doi.org/10.4000/geomorphologie.12139

Kazatchenko, E., & Mousatov, A. (2002). Primary and secondary porosity estimation of carbonate formations using total porosity and the formation factor, *SPE Journal, SPE 77787*, San Antonio Texas, 29 Septembre–2 octobre 2002, 6 pp.

Kemna, A., Binley, A., Cassiani, G., Niederleithinger, E., Revil, A., Slater, L., et al. (2012). An overview of the spectral induced polarization method for near-surface applications. *Near Surface Geophysics*, *10*, 453–468. https://doi.org/10.3997/1873-0604.2012027

Kulenkampff, J., & Schopper, J. R. (1988).Low frequency complex conductivity – a means for separating volume and interlayer conductivity. In: *Eleventh European Formation Evaluation Symposium – Transactions*. SPWLA, Oslo.

Labrecque, D., & Daily, W. (2008). Assessment of measurement errors for galvanic-resistivity electrodes of different composition. *Geophysics*, *73*(2), F55–F64. https://doi.org/10.1190/1.2823457

Lee, S. S., Heberling, F., Sturchio, N. C., Eng, P. J., & Fenter, P. (2016). Surface charge of the calcite (104) terrace measured by Rb^+ adsorption in aqueous solutions using resonant anomalous X-ray reflectivity. *Journal of Physical Chemistry C*, *120*(28), 15216–15223. https://doi.org/10.1021/acs.jpcc.6b04364

Leroy, P., Li, S., Jougnot, D., Revil, A., & Wu, Y. (2017). Modeling the evolution of spectral induced polarization during calcite precipitation on glass beads. *Geophysical Journal International*, *209*(1), 123–140. https://doi.org/10.1093/gji/ggx001

Leroy, P., & Revil, A. (2009). A mechanistic model for the spectral induced polarization of clay materials. *Journal of Geophysical Research*, *114*, 1–21. https://doi.org/10.1029/2008jb006114

Leroy, P., Revil, A., Kemna, A., Cosenza, P., & Ghorbani, A. (2008). Complex conductivity of water-saturated packs of glass beads. *Journal of Colloid and Interface Science*, *321*(1), 103–117. https://doi.org/10.1016/j.jcis.2007.12.031

Li, S., Leroy, P., Heberling, F., Devau, N., Jougnot, D., & Chiaberge, C. (2016). Influence of surface conductivity on the apparent zeta potential of calcite. *Journal of Colloid and Interface Science*, *468*, 262–275. https://doi.org/10.1016/j.jcis.2016.01.075

Loke, M. H., & Barker, R. D. (1996). Rapid least-squares inversion of apparent resistivity pseudosections by a quasi-Newton method. *Geophysical Prospecting*, *44*, 131–152. https://doi.org/10.1111/j.1365-2478.1996.tb00142.x

Maineult, A., Jougnot, D., & Revil, A. (2018). Variations of petrophysical properties and spectral induced polarization in response to drainage and imbibition: A study on a correlated random tube network. *Geophysical Journal International*, *212*(2), 1398–1411. https://doi.org/10.1093/gji/ggx474

Norbisrath, J. H., Eberli, G. P., Shen, S., & Weger, R. J. (2018). Complex resistivity spectra for estimating permeability in dolomites from the Mississippian Madison Formation, Wyoming. *Marine and Petroleum Geology*, *89*, 479–487. https://doi.org/10.1016/j.marpetgeo.2017.10.014

Rai, K., Rawat, N. S., Verma, R. P., & Kumar, P. (2004). High resolution reservoir characterization of bassin limestone in Neelam Field of Mumbai Offshore Basin using FMS image data, 5th Biennial SPG Conference & Exposition on Petroleum Geophysics, Hyderabad, 2004, India, PP. 124–134.

Regnet, C., David, C., Robio, P., & Menéndez, B. (2019). Microstructures and physical properties in carbonate rocks: A comprehensive review. *Marine and Petroleum Geology*, *103*, 366–376. https://doi.org/10.1016/j.marpetgeo.2019.02.022

Revil, A., Coperey, A., Deng, Y., Cerepi, A., & Seleznev, N. (2018). Complex conductivity of tight sandstones. *Geophysics*, *83*(2), E55–E74. https://doi.org/10.1190/GEO2017-0096.1

Revil, A., Coperey, A., Shao, Z., Florsch, N., Fabricius, I. L., Deng, Y., et al. (2017a). Complex conductivity of soils. *Water Resources Research*, *53*(8), 7121–7147. https://doi.org/10.1002/2017WR020655

Revil, A., Le Breton, M., Niu, Q., Wallin, E., Haskins, E., & Thomas, D. M. (2017b). Induced polarization of volcanic rocks. 1. Surface versus quadrature conductivity. *Geophysical Journal International*, *208*, 826–844. https://doi.org/10.1093/gji/ggw444

Revil, A., Le Breton, M., Niu, Q., Wallin, E., Haskins, E., & Thomas, D. M. (2017c). Induced polarization of volcanic rocks. 2. Influence of pore size and permeability. *Geophysical Journal International*, *208*, 814–825. https://doi.org/10.1093/gji/ggw382

Revil, A., Soueid Ahmed, A., Coperey, A., Ravanel, L., Sharma, R., & Panwar, N. (2020). Induced polarization as a tool to characterize shallow landslides. *Journal of Hydrology*, *589*, 125369. https://doi.org/10.1016/j.jhydrol.2020.125369

Ricci, M., Spijker, P., Stellacci, F., Molinari, J. F., & Voitchovsky, K. (2013). Direct visualization of single ions in the Stern layer of calcite. *Langmuir*, *29*, 2207–2216. https://doi.org/10.1021/la3044736

Saneiyan, S., Ntarlagiannis, D., & Colwell, F. (2021). Complex conductivity signatures of microbial induced calcite precipitation, field and laboratory scales. *Geophysical Journal International*, *224*(3), 1811–1824. https://doi.org/10.1093/gji/ggaa510

Sharma, R., Prasad, M., Surve, G., & Katiyar, G. C. (2006).On the applicability of Gassmann model in carbonates. *SEG/New Orleans Annual Meeting*.

Stern, O. (1924). Zur Theorie der elektrolytischen doppelschicht, 30(21–22), 508–516. https://doi.org/10.1002/bbpc.192400182

Stipp, S. L. S. (1999). Toward a conceptual model of the calcite surface: Hydration, hydrolysis, and surface potential. *Geochimica et Cosmochimica Acta*, *63*, 3121–3131. https://doi.org/10.1016/s0016-7037(99)00239-2

van Cappellen, P., Charlet, L., Stumm, W., & Wersin, P. (1993). A surface complexation model of the carbonate mineral-aqueous solution interface. *Geochimica et Cosmochimica Acta*, *57*, 3505–3518. https://doi.org/10.1016/0016-7037(93)90135-j

Van Voorhis, G. D., Nelson, P. H., & Drake, T. L. (1973). Complex resistivity spectra of porphyry copper mineralization. *Geophysics*, *38*(1), 49–60. https://doi.org/10.1190/1.1440333

Vinegar, H., & Waxman, M. (1984). Induced polarization of shaly sands. *Geophysics*, *49*(8), 1267–1287. https://doi.org/10.1190/1.1441755

Wan, W., Tang, X., & Huang, Q. (2019). Influence of induced polarization effects on 3D land CSEM sounding. *Progress in Geophysics*, *34*(6), 2328–2335.

Weller, A., Slater, L., Binley, A., Nordsiek, S., & Xu, S. (2015). Permeability prediction based on induced polarization: Insights from measurements on sandstone and unconsolidated samples spanning a wide permeability range. *Geophysics*, *80*(2), D161–D173. https://doi.org/10.1190/geo2014-0368.1

Weller, A., Slater, L., & Nordsiek, S. (2013). On the relationship between induced polarization and surface conductivity: Implications for petrophysical interpretation of electrical measurements. *Geophysics*, *78*(5), D315–D325. https://doi.org/10.1190/geo2013-0076.1

Winn, R. H. (1957). Log interpretation in heterogeneous carbonate reservoirs. *Society of Petroleum Engineers*. https://doi.org/10.2118/818-G

Wolthers, M., Charlet, L., & Van Cappellen, P. (2008). The surface chemistry of divalent metal carbonate minerals; a critical assessment of surface charge and potential data using the charge distribution multi-site ion complexation model. *American Journal of Science*, *308*, 905–941. https://doi.org/10.2475/08.2008.02

Wu, Y., Hubbard, S., Williams, K. H., & Ajo-Franklin, J. (2010). On the complex conductivity signatures of calcite precipitation. *Journal of Geophysical Research*, *115*, G00G04. https://doi.org/10.1029/2009jg001129

Zimmermann, E., Kemna, A., Berwix, J., Glaas, W., Münch, H. M., & Huisman, J. A. (2008). A high-accuracy impedance spectrometer for measuring sediments with low polarizability. *Measurement Science and Technology*, *19*(10), 105603. https://doi.org/10.1088/0957-0233/19/10/105603